Kinematic Analysis of white dwarfs based on *Gaia* astrometry

Bachelorarbeit aus der Physik

Vorgelegt von
Markus Dimpel
17.10.2018

Friedrich-Alexander-Universität Erlangen-Nürnberg

Betreuer: Prof. Dr. Ulrich Heber und Dr. Roberto Raddi

Contents

1. Introduction

The precise distribution of stellar mass throughout the main components of the Milky Way – thin disk, thick disk and halo – is still unclear. The study of white dwarfs' kinematics is a valuable tool in determining the fraction of total mass of our Galaxy contained in the form of thin-disk, thick-disk and halo white dwarfs. As the *Gaia* mission recently published high-precision measurements of the astrometric parameters of over one million objects in the Milky Way, it is tempting to re-analyze the sample of white dwarfs, already studied by Pauli et al. (2006), and re-classify their membership to the Galactic populations.

1.1. White dwarfs

White dwarfs are the electron-degenerate remnants of stars with masses of about 1 to $10\,M_\odot$ (Althaus et al. 2010), where $M_\odot$ denotes the solar mass $M_\odot = 1.99 \cdot 10^{30}\,\mathrm{kg}$. During most of their lifetime, stars burn hydrogen into helium within their cores via nuclear fusion. The pressure of the hot gas inside the stars balances the gravitational force, so that they do not contract. Once the star runs out of hydrogen in the core, its core starts to shrink as the gravitational pressure becomes dominant. Due to the contraction, the temperaturs of the gas surrounding the core becomes hot enough for hydrogen fusion (shell burning). This leads to an expansion of the outer layers of the star and it becomes a so called *red giant*. At some point the temperatures inside the core are hot enough ($\sim 10^8\,\mathrm{K}$) to fuse the helium into carbon and oxygen. Once sufficient amounts of carbon and oxygen are produced, two shell-burning occur, where helium is fused in the inner shell and hydrogen in the outer one. At this point, the core is already degenerate and does not shrink. Thus it does not get hot enough to fuse the carbon and oxygen. The stellar envelope expands again and cools down. The formation of dust favours strong mass loss and finally, a so called *planetary nebula* is formed. The remaining carbon-oxygen core is a white dwarf.
White dwarfs have a very thin atmosphere around their carbon-oxygen core. This atmosphere is – in most cases – either hydrogen or helium dominated. The former are called DA white dwarfs, the latter DB white dwarfs. (Althaus et al. 2010)
Once they are formed, white dwarfs do not sustain further nuclear fusion and slowly cool down irradiating their stored energy. For the rest of their lifetime, white dwarfs are about $10\,\mathrm{mag}$ fainter than their visual luminosity on the main sequence.

1.2. Galactic structure

The Milky Way Galaxy is a complex dynamic structure, where different stellar populations, gas and dust interact with each other. It is a spiral galaxy that is estimated to include a baryonic mass of $\sim 10^{11}\,M_\odot$. At its center, a massive black hole, Sgr A*, is located, which has a mass $M = (3.6 \pm 0.3)\,M_\odot$. The Milky Way can be divided mainly into the galactic disk and the halo. The disk is the most massive stellar component of the Galaxy, containing its spiral arms and reaching out to radii of about $15\,\mathrm{kpc}$. The stellar mass of the disk is believed to be $\sim 5 \cdot 10^{10}\,M_\odot$. The vertical density profile of the disk can be accurately fitted by the sum of two exponentials. This suggests the separation of the disk into two compenents, the **thin**

disk and the **thick disk**, with scale heights $h_{\mathrm{thin}} = 300\,\mathrm{pc}$ and $h_{\mathrm{thick}} = 900\,\mathrm{pc}$. The thin disk is a region of ongoing star formation and thus contains stars of a wide range of ages, which in general have high metallicities. The orbits of stars in the thin disk are of high angular momentum and are almost circular. At the position of the Sun, the thin disk rotates at a mean velocity $v_{\mathrm{LSR}} \approx 220\,\mathrm{km/s}$ (LSR: Local Standard of Rest). The average rotation of the thick disk lags behind that of the thin disk. In general, thick-disk stars have orbits of lower angular momenta than thin-disk stars and have lower metallicities. The Galactic **halo** is nearly spherical and extends to radii of $\sim 100\,\mathrm{kpc}$. It has no net rotation ($V_{\mathrm{rot}} = 0$), the halo stars can even move in the opposite direction than the disk and often have very eccentric orbits. The halo contains mainly old and metal-poor stars and is studded with globular clusters. (Wyse 2004; Turon et al. 2008)
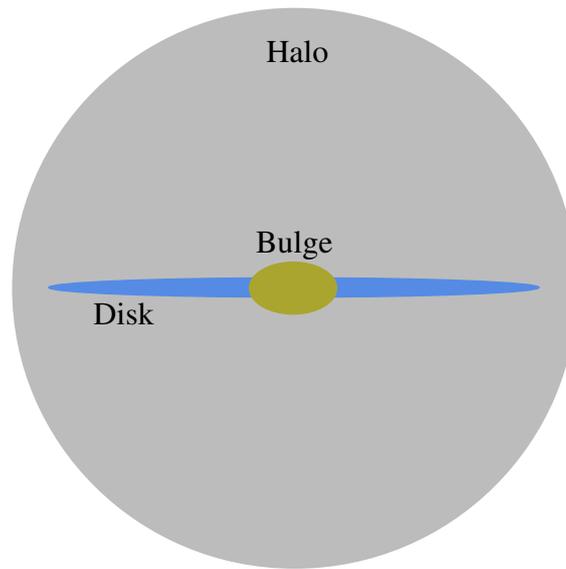

Figure 1: Sketch of the Milky Way structure.

2. Astrometry

Coordinate reference systems are used to map the positions of celestial objects on the sky, in order to make them unequivocally identifiable by different observers. This was of great importance for example for sailors, who had to follow given routes on the sea. In modern astronomy the highest precision is required to study transient phenomena, and to accurately trace the relative motions of stars.

2.1. Equatorial coordinate system

The equatorial coordinate system is best suited to describe the coordinates of an object on the celestial sphere independent of the location of the observer on Earth. Its origin is the center of Earth and its fundamental plane is the projection of Earth's equator onto the celestial sphere, called the celestial equator. The pair of coordinates in the equatorial system is defined as *right ascension* and *declination*.

Right ascension is analogous to terrestial longitude. The right ascension of an object on the celestial sphere is the angular distance measured eastward along the celestial equator, with the vernal equinox of the Sun, which is the intersection of the celestial equator and the ecliptic, as its origin. The ecliptic is the projection of the Earth's orbit onto the celestial sphere. The right ascension, which is usually abbreviated with α or "ra", is either measured in degrees or in hours, minutes and seconds, where one hour corresponds to $15°$. Its value can range from $0°$ to $360°$ and $0\,\mathrm{h}$ to $24\,\mathrm{h}$, respectively.

The declination, abbreviated with δ or "dec", measures the angular distance of an object perpendicular to the celestial equator with a positive sign towards the celestial north pole and a negative sign towards the celestial south pole. It is given in degrees and ranges from $-90°$ to $90°$, analogous to terrestial latitude.

The description of the coordinates above is slightly simplified. The slow motion of Earth's axis, the so called *precession*, causes the coordinate system to change with a period of about $26\,000$ years. Additionally there is a small oscillation of Earth's axis, the so called *nutatuion*. These two effects require the definition of a so called epoch, which specifies the equinox of a particular date. Since 1984 the Julian epoch *J2000* is in use, which corresponds to the date January 1st 2000, $12\,\mathrm{h}$ UT.

The celestial equator and the ecliptic, and thus the origin of the coordinate tuple, are fixed with respect to the stars on the celestial sphere when regarding short enough time scales so that the effects of precession and nutation can be neglected. Thus the right ascension and declination of a specific object are independent of the observers position on Earth.

2.2. Galactic coordinate system

The Galactic coordinate system is a spherical coordinate system, which has the Sun at its center. The galactic longitude l measures the angular distance of an object eastward along the galactic equator with the galactic center as its origin ($l = 0$). It is given in degrees, analogous to the terrestrial longitude, and ranges from $0°$ to $360°$.
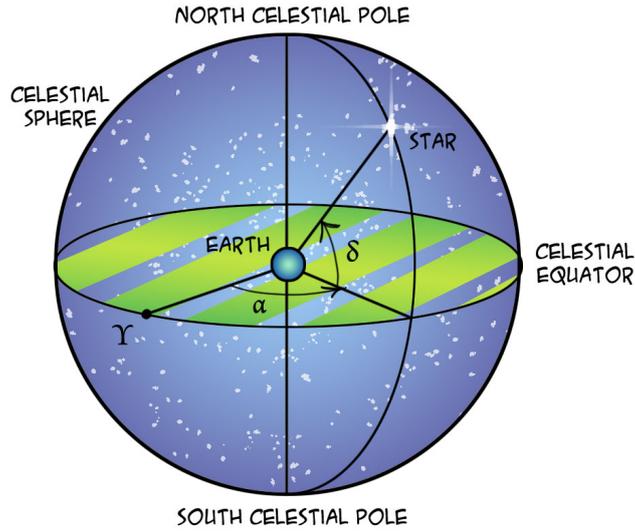
Figure 2: Sketch of the equatorial coordinate system (Υ: vernal eqinox, α: right ascension, δ: declination) (equ 2013).

The Galactic latitude b measures the angle of an object perpendicular to the galactic plane, with a positive sign towards the north and a negative sign towards the south. It is analogous to terrestrial latitude and ranges from $-90°$ to $90°$.

The galactic coordinates l and b can be calculated from the equatorial coordinates α and δ by a simple coordinate transformation.
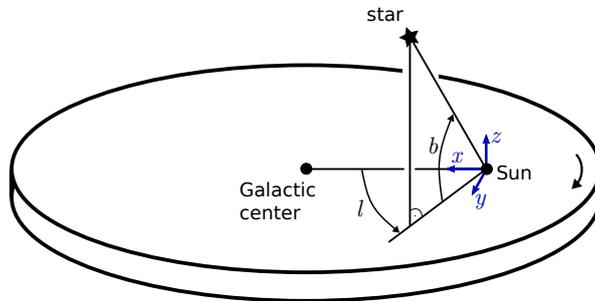
Figure 3: Sketch of the galactic coordinate system.

When the distance d of a star is known, the spherical coordinates can be transformed into heliocentric cartesian coordinates x, y and z:

$$\begin{pmatrix} x \\ y \\ z \end{pmatrix}_{HC} = d \cdot \begin{pmatrix} \cos b \cos l \\ \cos b \sin l \\ \sin b \end{pmatrix} \tag{1}$$

The x-axis points towards the galactic center, the y-axis in the direction of the solar orbit and the z-axis towards the north galactic pole.

5

Shifting the x-axis by the distance of the Sun from the Galactic center, r_0, results in the transformation from the heliocentric to the galactocentric system:

$$\begin{pmatrix} X \\ Y \\ Z \end{pmatrix}_{GC} = \begin{pmatrix} x - r_0 \\ y \\ z \end{pmatrix}. \tag{2}$$

2.3. Parallax

One method to measure the distance of an object inside the Milky Way is the annual trigonometric parallax, which is defined as the angular displacement of a nearby star with respect to the background, due to Earth's orbital motion, see Figure 4. Within one year – corresponding to the orbit of the Earth around the Sun – the star moves on an ellipse on the celestial sphere. By measuring the parallax angle p one can easily estimate the object's distance d using simple trigonometry:

$$p \approx \tan p = \frac{1\,\text{AU}}{d}. \tag{3}$$

If the parallax angle is given in arcseconds, the distance in parsecs can be obtained via

$$d = \frac{1}{p}. \tag{4}$$

In general stars have some transversal velocity relative to the Sun. For the method described above, this velocity is assumed to be negligible. However, all stars move, so that the parallax has to be measured over a timespan of multiple years in order to be able to disentangle the effect of parallax and relative velocity, as the star will move on a spiral instead of an ellipse, see Figure 5.
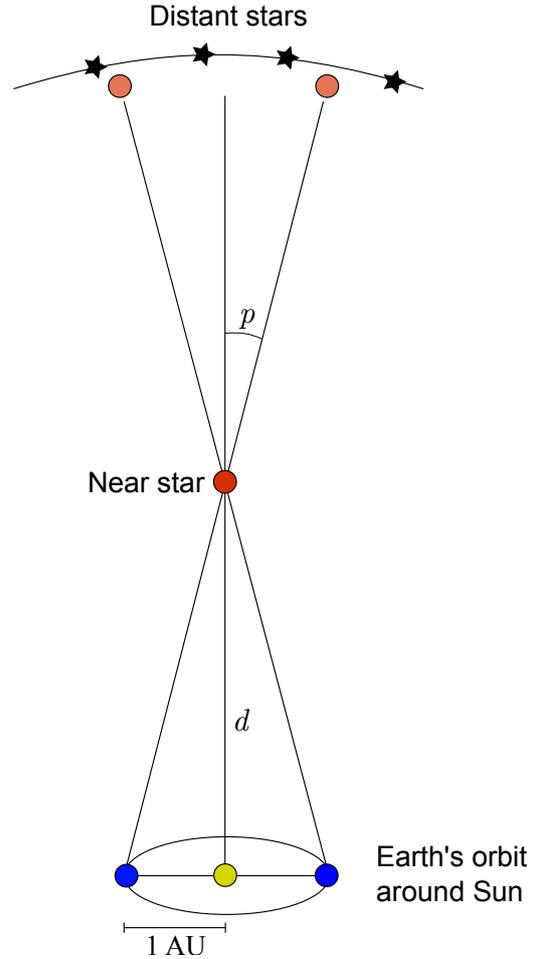
Figure 4: Visualised definition of the parallax angle p.

2.4. Proper motion and radial velocity

As mentioned above, stars – in general – have a velocity v relative to the solar system, which can be divided into a transversal (v_t) and a radial part (v_r):

6
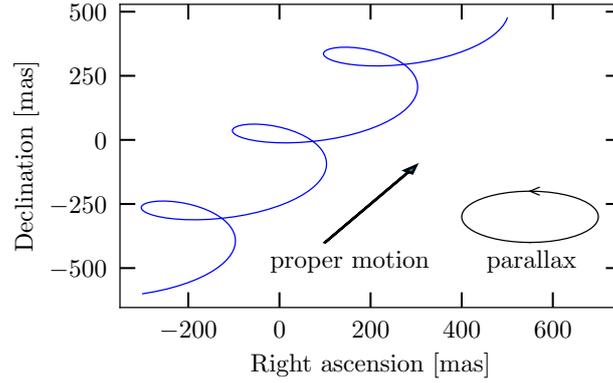
Figure 5: Superposition of parallax and proper motion.

$$v = \sqrt{v_{\text{t}}^2 + v_{\text{r}}^2}. \tag{5}$$

Due to the transversal velocity component, their coordinates on the celestial sphere change with time. This angular movement on the celestial sphere is called *proper motion* (μ) and can be devided into two components, the proper motion in the direction of right ascension (μ_α) and declination (μ_δ), respectively. Multiplied by the distance, d, between Earth and the respective star, the proper motion results in the transverse velocity:

$$v_{\text{t}} = d \cdot \mu = d \cdot \sqrt{\mu_\delta^2 + \mu_\alpha^2 \cdot \cos^2 \delta} \tag{6}$$

The proper motion of a star can be obtained by measuring its coordinates at two different points in time and is usually given in (milli-)arcseconds per year. A sketch of a stars velocity relative to Earth can be seen in Figure 6.
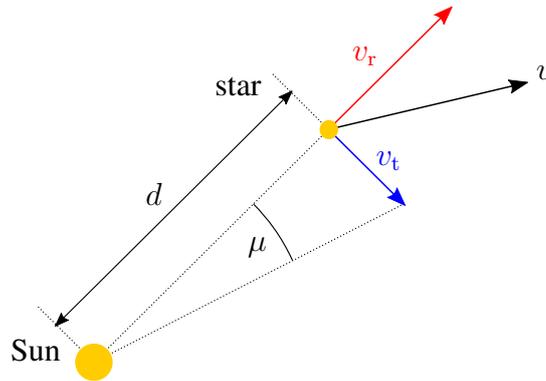
Figure 6: Sketch of proper motion and radial velocity of a star.

The radial velocity component of a star does not affect its position on the sky, but it affects the emitted light via the Doppler effect. Stars that approach or move far away from the Sun will

have their spectral energy distributions blue- or red-shifted. Hence, stellar radial velocities can be measured by determining the wavelength shift of spectral lines, $\Delta\lambda$, either in absorption or emission, with respect to those measured in the laboratory, λ, via

$$\frac{\Delta\lambda}{\lambda} = \frac{v_\mathrm{r}}{c}. \tag{7}$$

The radial velocity and proper motions of an object can be transformed into the helicentric, galactic velocities u, v and w. By adding the rotation of the Local Standard of Rest, r_LSR, and the velocity of the Sun in the heliocentric, galactic coordinates, $(U_\odot,\ V_\odot,\ W_\odot)^\mathrm{T}$, they can be transformed into galactocentric velocities:

$$\begin{pmatrix} U \\ V \\ W \end{pmatrix}_\mathrm{GC} = \begin{pmatrix} u \\ v \\ w \end{pmatrix}_\mathrm{HC} + \begin{pmatrix} U_\odot \\ V_\odot + v_\mathrm{LSR} \\ W_\odot \end{pmatrix}. \tag{8}$$

2.5. The *Gaia* mission

The astrometric data used for the analysis in this thesis was provided by the *Gaia* mission of the *European Space Agency* (ESA). The *Gaia* satellite was launched on 19 December 2013 and arrived a few weeks later at its point of operation, the second Lagrange point of the Sun-Earth-Moon system (Gaia Collaboration et al. 2016).

The "Second Data Release" of the *Gaia* mission, referred to as *Gaia* DR2, was released on 25 April 2018 and provides a five-parameter astrometric solution for over 1.3 billion objects, including their positions on the celestial sphere, parallaxes and proper motions (Gaia Collaboration et al. 2018b). Also the radial velocities for over 7 million objects brighter than 12th magnitude in the G band are provided (Gaia Collaboration et al. 2018b).

In addition to precise astrometry, *Gaia* DR2 also provides photometric data. The apparent magnitudes in the G, G_BP ($330\,\mathrm{nm} - 680\,\mathrm{nm}$) and G_RP ($630\,\mathrm{nm} - 1050\,\mathrm{nm}$) bands are available for over 1.3 billion objects (Gaia Collaboration et al. 2018b).

3. White dwarf sample

The sample of white dwarfs examined in this thesis originates from the European Southern Observatory (ESO) **S**N Ia **P**rogenitor surve**Y** (SPY) and consists of the 398 white dwarfs, analyzed by Pauli et al. (2006), and 252 unpublished white dwarfs, adding up to a total size of the sample of 650 stars.

3.1. The SPY survey

Close double degenerate (DD) binaries, consisting of two white dwarfs orbiting around each other, are potential progenitors of Supernova explosions of type Ia. SPY aimed to discover such binary systems by taking high resolution spectra with the UV-Visual Echelle Spectrograph (UVES) of the ESO Very Large Telescope (VLT) and analyze them for radial velocity variations. The targets for the SPY project were obtained from five sources: the white dwarf catalog of McCook & Sion (1999), the Hamburg ESO Survey (HES), the Hamburg Quasar Survey, the Montreal-Cambridge-Tololo survey (MCT) and the Edinburgh-Cape survey (EC). By 2005 SPY already detected over 100 new white dwarf binaries, drastically increasing the number of known DDs, as there were only 18 known DDs before the start of SPY in the year 2000. (Napiwotzki et al. 2001, 2003a,b, 2005)

3.2. Physical parameters

The effective temperature, T_{eff}, and surface gravity, $\log g$, of a star are directly related to its physical parameter: mass M, radius R and luminosity L. The effective temperature of a star is defined as the temperature of a black body irradiating the same power per unit area as the star. Thus, it is a function of stellar radius and luminosity:

$$\sigma T_{\mathrm{eff}}^4 = \frac{L}{4\pi R^2},\tag{9}$$

where σ denotes the Stefan-Boltzmann constant $\sigma = 5.67 \cdot 10^{-5}\,\mathrm{erg\,cm^{-2}\,s^{-1}\,K^{-4}}$. The surface gravity

$$\log g = \log\left(\frac{GM}{R^2}\right)\tag{10}$$

however, is a function of stellar mass and radius. $G = 6.67 \cdot 10^{-8}\,\mathrm{dyn\,cm^2\,g^{-2}}$ is the gravitational constant. (Smalley 2005)

3.3. Gravitational redshift

Because white dwarfs are compact objects, their surface gravities are significantly greater than those of main-sequence stars. One can use the conservation of energy and the General Relativity Theory to show, that the frequency of light, ν, emitted by a source in a strong gravitational field, is shifted and is registered by an observer located far enough from the object as light with a different frequency ν_∞:

$$\frac{\nu_\infty - \nu}{\nu} = -\frac{GM}{Rc^2},\tag{11}$$

where c denotes the speed of light. As all quantities on the right side are positive, the observed frequency ν_∞ is smaller than the emitted one, ν, and the light is red-shifted. Thus, this effect is called *Gravitational redshift*. (Evans & Dunning-Davies 2004)

As the radial velocity of a white dwarf is measured via the wavelength-shift of the white dwarf's spectrum, the measured radial velocity has to be blue-shifted by a value of

$$v_G = \frac{GM}{Rc}.\tag{12}$$

3.4. Examining *Gaia* measurements

Given that the *Gaia* astrometry is highly precise for nearby stars, such as white dwarfs, I searched for *Gaia* data by cross-matching the SPY sample with *Gaia*, using the Virtual observatory tools offered by *Topcat* (Taylor 2005). To validate the cross-match outcome, let us first look at the comparison between the proper motions of our sample, provided by *Gaia* DR2, and the ones used in Pauli et al. (2006). In Figure 7 and 8, these comparisons are plotted for the two components of proper motions of the 398 stars from Pauli et al. (2006), respectively.

On average, the *Gaia* errors are smaller than the errors on the values used by Pauli et al. (2006) by a factor of almost 100, as can be seen in Table 1. For the majority of stars, I found a very accurate one-to-one correlation.

Table 1: Mean errors on μ_α and μ_δ from Pauli et al. (2006) and *Gaia*.

	σ_{μ_α} [mas/yr]	σ_{μ_δ} [mas/yr]
Pauli	7	7
Gaia	0.13	0.11

However, there are two outliers with differences of the order of some hundred $\mathrm{mas/yr}$. For WD 0255−705 *Gaia* measures $\mu_{\alpha,\mathrm{Gaia}} = (654.48 \pm 0.05)\,\mathrm{mas/yr}$ and $\mu_{\delta,\mathrm{Gaia}} = (-112.37 \pm 0.05)\,\mathrm{mas/yr}$, while Pauli et al. (2006) have $\mu_{\alpha,\mathrm{Pauli}} = (883 \pm 85)\,\mathrm{mas/yr}$ and $\mu_{\delta,\mathrm{Pauli}} = (-401 \pm 85)\,\mathrm{mas/yr}$, and for HS 1527+0614 $\mu_{\delta,\mathrm{Gaia}} = (-91.99 \pm 0.11)\,\mathrm{mas/yr}$ and $\mu_{\delta,\mathrm{Pauli}} = (-666 \pm 41)\,\mathrm{mas/yr}$. These significant differences in proper motion suggest a high chance that the respective star's membership to Galactic populations will differ from that assigned by Pauli et al. (2006).

Similarly, the deviations of the distances of the stars, estimated via the parallaxes measured by *Gaia*, from the spectroscopic distances, obtained from SPY spectra, are plotted versus the spectroscopic distances, which were used for the analysis by Pauli et al. (2006), in Figure 9. The parallaxes obtained by *Gaia* are in good agreement with the spectroscopic distances below $200\,\mathrm{pc}$. With increasing distance, however, the deviations become larger, up to differences of
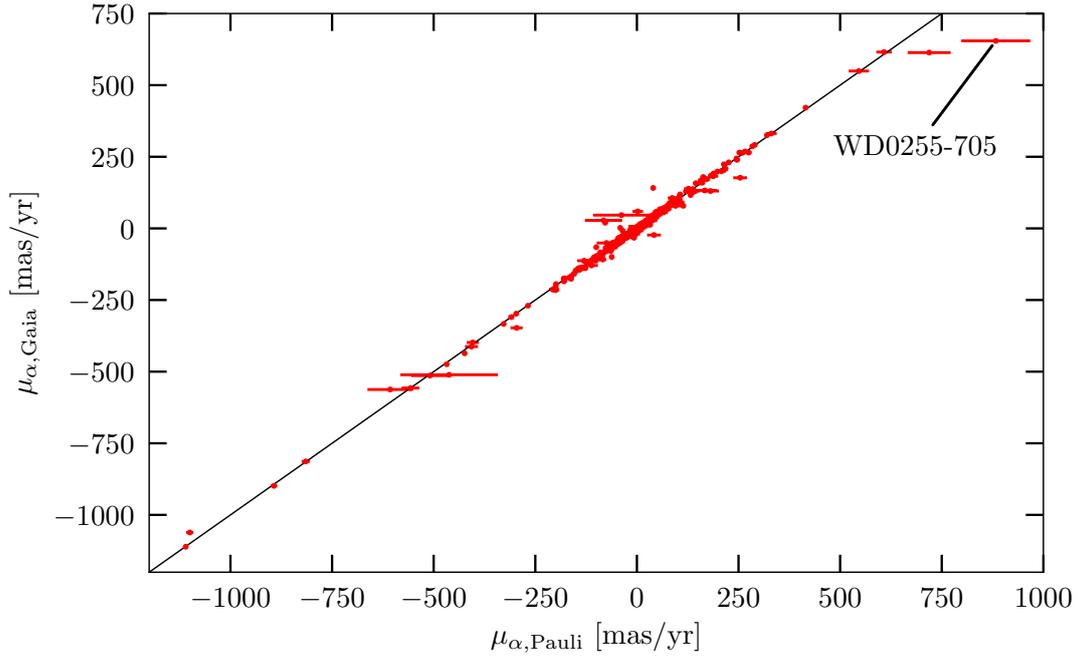
Figure 7: Proper motions in the direction of rigth ascension measured by *Gaia* versus the ones used by Pauli et al. (2006). Individual objects discussed in the text are labeled with their names.
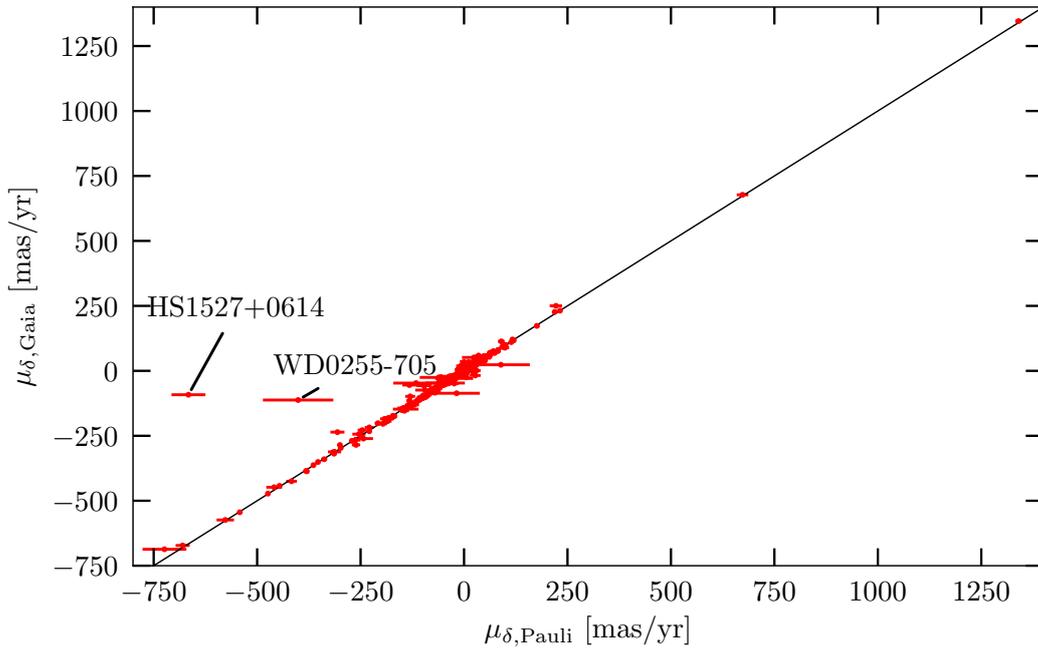
Figure 8: Proper motions in the direction of declination measured by *Gaia* versus the ones used by Pauli et al. (2006). Individual objects discussed in the text are labeled with their names.
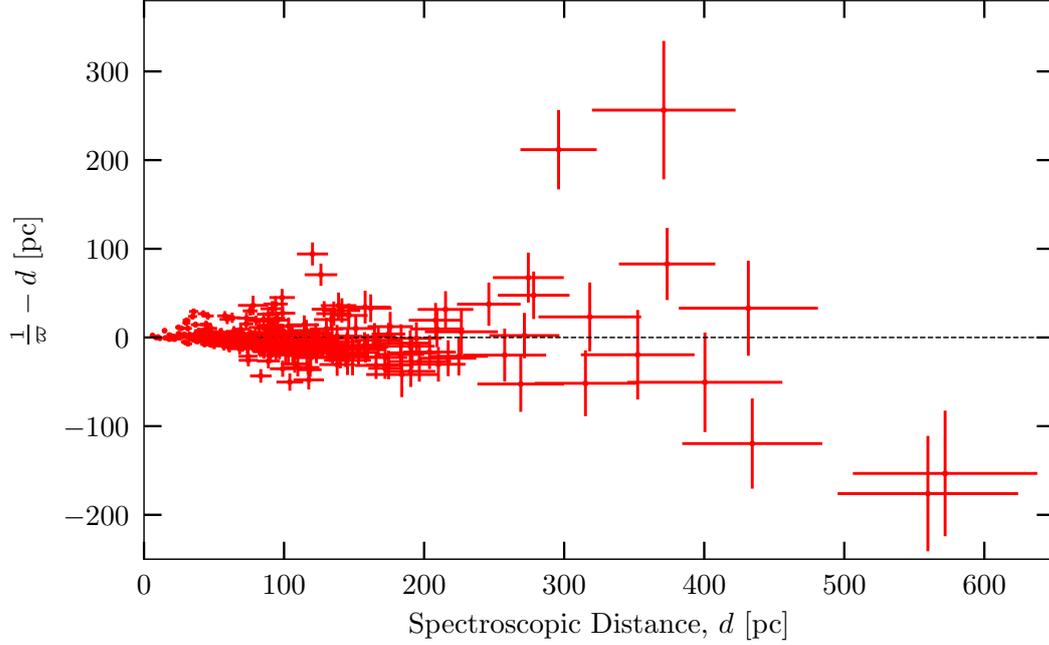
Figure 9: Distance estimates via *Gaia* parallaxes versus spectroscopic distances from SPY. Individual objects discussed in the text are labeled with their names.

almost $300\,\mathrm{pc}$. There is one extreme outlier, WD 2204+071 (not shown in Figure 9), which, according to *Gaia*, has a distance of $\sim 1.75\,\mathrm{kpc}$, but the spectroscopic distance is $\sim 150\,\mathrm{pc}$. A possible reason for this large discrepancy can be seen in the Hertzsprung-Russell diagram. The HR diagram of the full sample of 650 white dwarfs can be seen in Figure 10, where the absolute *Gaia* magnitude

$$M_G = m_G - 5 \cdot \left(\log_{10} \tfrac{1}{\varpi} + 1 \right), \tag{13}$$

calculated from the apparent *Gaia* G magnitude, m_G, and parallax measurements from *Gaia* DR2, ϖ, is plotted versus the color, $G_{\mathrm{BP}} - G_{\mathrm{RP}}$, of the star. Also, three cooling tracks of DA white dwarfs with different $\log g$ values, obtained by convolving synthetic spectra of DA white dwarf models from Koester (2010) with *Gaia* DR2 passbands[1], are displayed.

Green and blue data points represent white dwarfs that have been identified as DD binaries by Napiwotzki et al. (in prep.) and references therein. For binaries represented by green data points, the orbit of the binary system has been solved and the system velocity γ has been determined by either Nelemans et al. (2005) or Morales-Rueda et al. (2005), respectively.

Most of the stars cluster in the region between the cooling tracks for $\log g = 7$ and $\log g = 9$, as expected for white dwarfs. The white dwarfs that are labeled with their names in the top left of Figure 10, however, have particularly low absolute magnitudes, which would suggest $\log g$'s significantly below 7.

In the astronomical database *Simbad*, WD 1123+189 is listed as a cataclysmic variable star

---

[1]https://www.cosmos.esa.int/web/gaia/iow_20180316

12
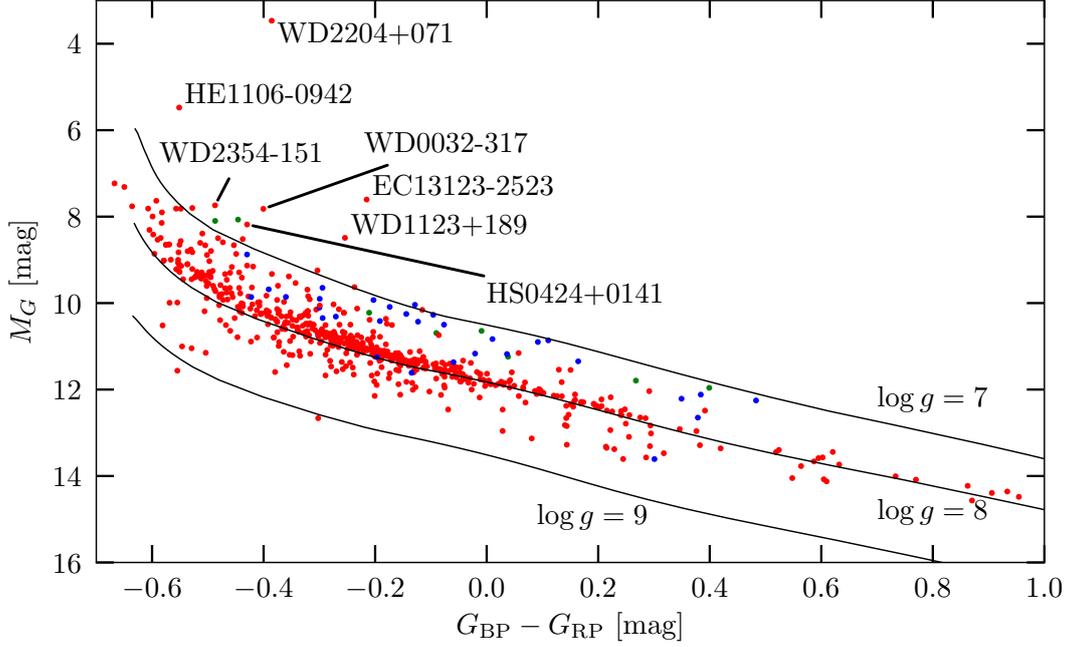
Figure 10: Absolute magnitude M vs. color $G_{\rm BP} - G_{\rm RP}$. Individual objects discussed in the text are labeled with their names.

and is thus part of a binary system. This explains the lower absolute magnitude of the star, as the secondary star contributes to the measured apparent magnitude of the white dwarf primary. WD 0032−317 has been identified as a binary candidate by Maoz & Hallakoun (2017).

WD 2204+071 is classified as a hot subdwarf in Zhang & Jeffery (2012). Just $4'$ below this hot subdwarf, but at the same right ascension, there is a white dwarf. It seems likely that the subdwarf was mistaken for this white dwarf. This would also explain the significant difference between the spectroscopic distance and the distance obtained from *Gaia*. The star HE 1106−0942 is also classified as a hot subdwarf (Stroeer et al. 2007) and thus is brighter than white dwarfs. These two subdwarfs have been removed from the sample.

For the stars HS 0424+0141, EC 13123−2523 and WD 2354−151 no references that would explain their particularly low absolute magnitudes have been found.

3.5. Radial velocities

Because *Gaia* cannot measure radial velocities of white dwarfs, they had to be obtained from a different source. Therefore, the radial velocities were provided by Napiwotzki et al. (in prep.). I interpolated the masses and radii of the white dwarfs, needed for the correction of the radial velocities for gravitational redshift, using $T_{\rm eff}$ and $\log g$ values, which have also been obtained from Napiwotzki et al. (in prep.). However, for fifteen stars, the $\log g$ values were outside of the grid limits. Thus these stars were left out of the interpolation process. Ten of those stars were also part of the sample of Pauli et al. (2006). Therefore, the radial velocities

13

used by Pauli et al. (2006) were used instead. The remaining five stars had to be left out of the analysis.

As mentioned earlier, in Napiwotzki et al. (in prep.) 39 stars are listed as likely or known white dwarf binaries. For 8 of them Nelemans et al. (2005) and Morales-Rueda et al. (2005) have solved the orbital parameters and determined the system velocity γ. Thus, for these stars, the radial velocity was replaced by the system velocity. The other 31 binary systems have been removed from the sample, as their measured radial velocities do not represent their radial space velocities.

There are three further white dwarfs, for which *Gaia* provided no parallax and proper motion measurements. Thus they also had to be removed from the sample, as the proper motions and the parallax are crucial for the kinematic analysis. This means, that altogether 41 stars were removed from the initial sample, leaving a final sample of 609 white dwarfs, that was used for the analysis.

Table 2: Overview of stars removed from the sample.

initial sample	subdwarfs	outside of grid limits	binaries without system velocity	missing parallax and proper motions	final sample
650	2	5	31	3	609

4. Classification scheme

As the sample examined in this thesis consists purely of white dwarfs, it is not possible to determine their population membership from metallicities (Pauli et al. 2006). This is why the white dwarfs have to be classified via kinematic criteria. These criteria have to be calibrated first, however, with the use of a calibration sample. For this purpose, Pauli et al. (2006) used a sample of 291 F and G main-sequence stars studied by Edvardsson et al. (1993), Fuhrmann (1998) and Fuhrmann (2004). In the following, the analysis of this calibration sample by Pauli et al. (2006) will be described briefly, as their results will be used in this thesis as well.

For the sample of main-sequence stars, the classification into thin-disk, thick-disk and halo stars was based on their Fe and Mg abundances. The different stellar populations were distinguished via the [Mg/Fe] vs. [Fe/H] diagram (Figure 11). Hereby, the abundance ratio [X/Y] denotes the logarithm of a star's number abundance compared to that of the Sun:

$$[\text{X/Y}] = \log_{10}\left(\frac{N_\text{X}}{N_\text{Y}}\right)_\text{star} - \log_{10}\left(\frac{N_X}{N_Y}\right)_\text{sun}. \tag{14}$$

N_X and N_Y are the particle fractions of the respective elements X and Y. In Figure 11, the 291 main-sequence stars are divided into halo, thick disk and thin disk, depending on their position in the abundance diagram. Halo stars were defined to have [Fe/H] < -1.05, thick-disk stars $-1.05 \leq$ [Fe/H] ≤ -0.3 and [Mg/Fe] ≥ 0.3, and thin-disk stars [Fe/H] > -0.3 and [Mg/Fe] ≤ 0.2. Pauli et al. (2006) omitted stars between the thin-disk and thick-disk region in Figure 11, marked as open triangles, and the metal-weak thick-disk stars, marked as open squares, to get a more distinct population.

For the thick- and thin-disk main-sequence stars Pauli et al. (2006) calculated the mean values and standard deviations of the U- and V-velocity components. These can be seen in Table 3. In the $U-V$ diagram (Figure 12) almost all stars with thin-disk abundance patterns are located inside the $3\sigma_\text{thin}$-contour and all halo stars are outside the $3\sigma_\text{thick}$-contour.

Table 3: Mean values and standard deviations of the U- and V-velocity components of the thin-disk and thick-disk main sequence stars (Pauli et al. 2006).

population	$\langle U_\text{ms} \rangle$ [km/s]	$\langle V_\text{ms} \rangle$ [km/s]	σ_{U_ms} [km/s]	σ_{V_ms} [km/s]
thin disk	3	215	35	24
thick disk	-32	160	56	45

Pauli et al. (2006) adopted the $J_Z - e$-diagram for determining the population membership of stars. Therefore, they integrated the stars' orbits in order to be able to calculate their eccentricities. In the $J_Z - e$-diagram, almost all stars of a specific population group together in an own region. This behaviour can be seen in Figure 13, where the Z-component of the angular momentum, J_Z, is plotted against the eccentricity, e, of the main-sequence stars' orbits. The thin-disk stars form a region with the shape of a triangle, located at low eccentricities and angular momenta around $1800 \, \text{kpc} \, \text{km} \, \text{s}^{-1}$, named region A. The majority of thick-disk stars has eccentricities above 0.27 and lower angular momenta (region B). The halo stars are located at
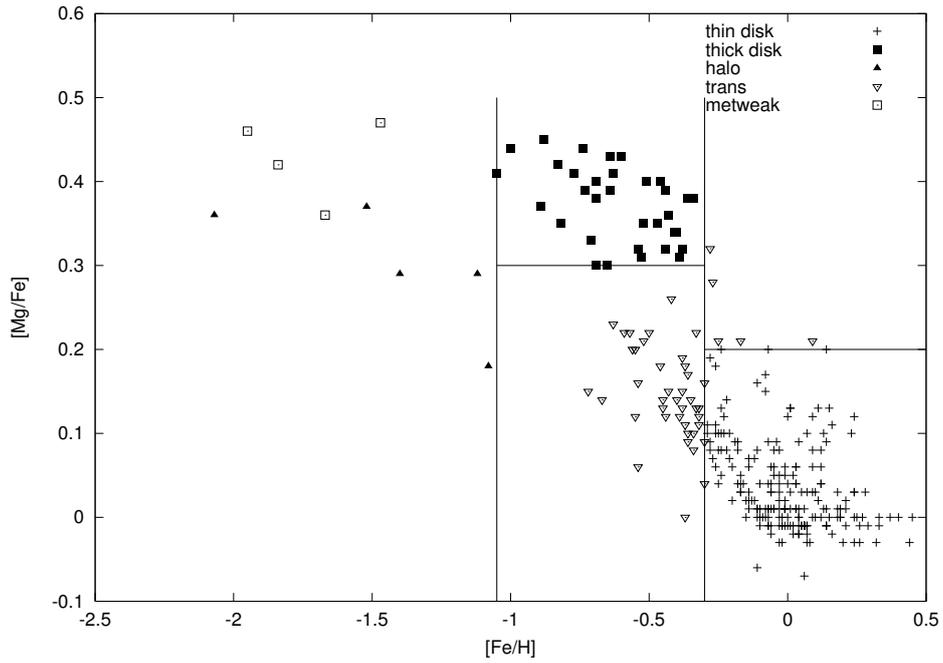
Figure 11: [Mg/Fe] vs. [Fe/H] abundance diagram of the calibration sample (Pauli et al. 2006).
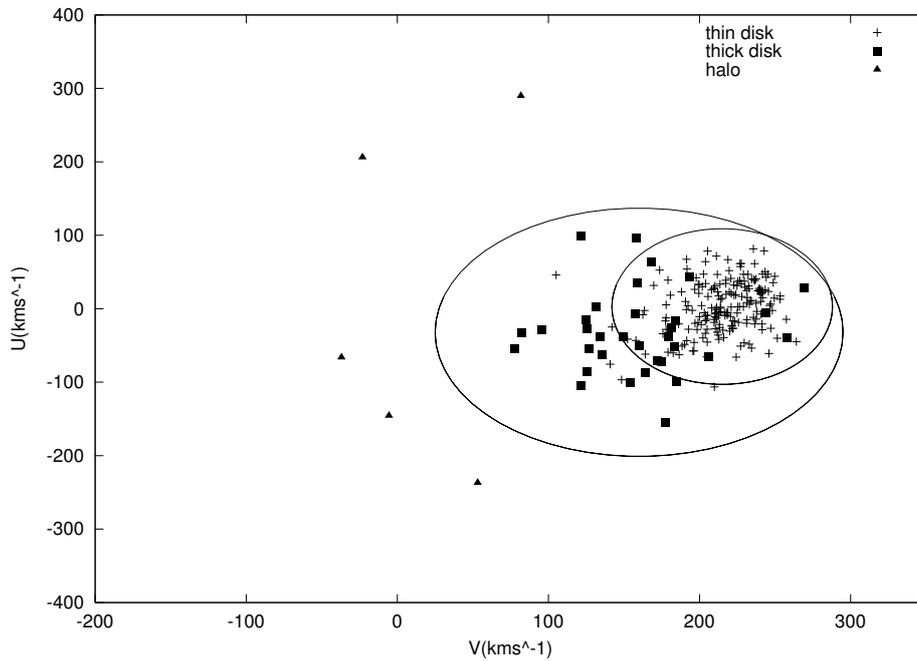
Figure 12: $U - V$-diagram of the calibration sample. Ellipses are the 3σ-limits of the thin disk (small ellipse) and thick disk (large ellipse) (Pauli et al. 2006).

16

the far right in the diagram, with very high eccentricities and even smaller angular momenta, called region C. (Pauli et al. 2006)
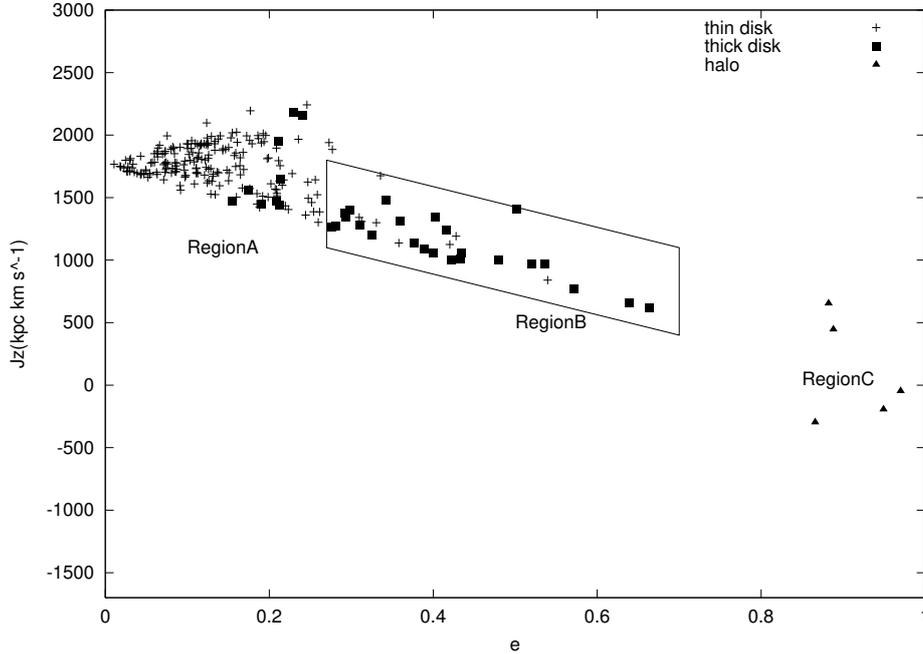
Figure 13: $J_Z - e$-diagram of the calibration sample (Pauli et al. 2006).

The third criterium is the Galactic orbit of the star, which Pauli et al. (2006) calculated for a Galactic potential from Allen & Santillan (1991). Exemplary plots of thin-disk, thick-disk and halo orbits can be seen in Figures 14 to 16.

The classification scheme developed by Pauli et al. (2006) assigns a classification value c to each star, which is defined as the sum of the three values c_{UV}, c_{J_Ze} and c_{orb}. These correspond to the positions in the $U-V$- and J_Z-e-diagram and the shape of the stars' orbits, respectively. Because the majority of stars belong to the thin disk, Pauli et al. (2006) were interested in identifying old white dwarfs as thick-disk and halo candidates. All stars that are located outside the $3\sigma_{\mathrm{thick}}$-limit in the $U-V$-diagram or in region C in the J_Z-e-diagram are defined as halo candidates. The remaining stars that are outside of the $3\sigma_{\mathrm{thin}}$-limit in the $U-V$-diagram or in region B in the J_Z-e-diagram are thick-disk candidates.

Then c_{UV}, c_{J_Ze} and c_{orb} are evaluated for the halo candidates. These values are either $+1$ if a halo membership is supported by the criterion or -1 if it is not. In other words: $c_{UV} = +1$ if the star is located outside the $3\sigma_{\mathrm{thick}}$-limit in the $U-V$-diagram, $c_{J_Ze} = +1$ if it is located in region C in the J_Z-e-diagram and $c_{\mathrm{orb}} = +1$ if the star has a halo orbit. If the sum $c = c_{UV} + c_{J_Ze} + c_{\mathrm{orb}} \geq +1$, the star is classified as a halo member, else as a thick-disk member.

The thick-disk candidates are treated analogously: $c_{UV} = +1$ if the star is located outside the $3\sigma_{\mathrm{thin}}$-limit, $c_{J_Ze} = +1$ if it is located in region B and $c_{\mathrm{orb}} = +1$ if the star has a thick-disk orbit. All thick-disk candidates with $c \geq +1$ are classified as thick-disk stars, the rest as thin-disk stars.

17
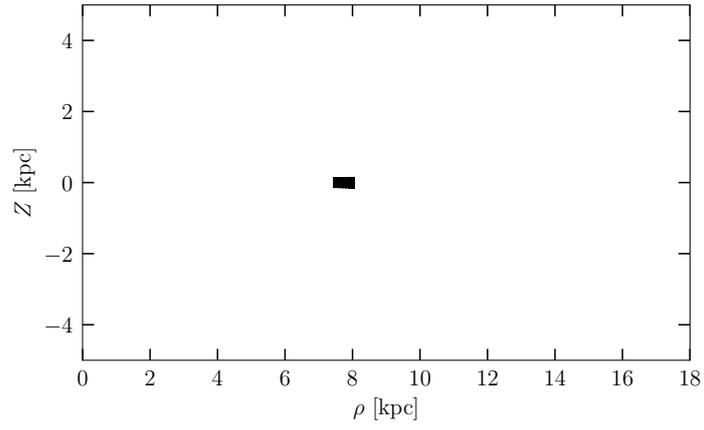
Figure 14: Thin-disk orbit of WD 1844-223.
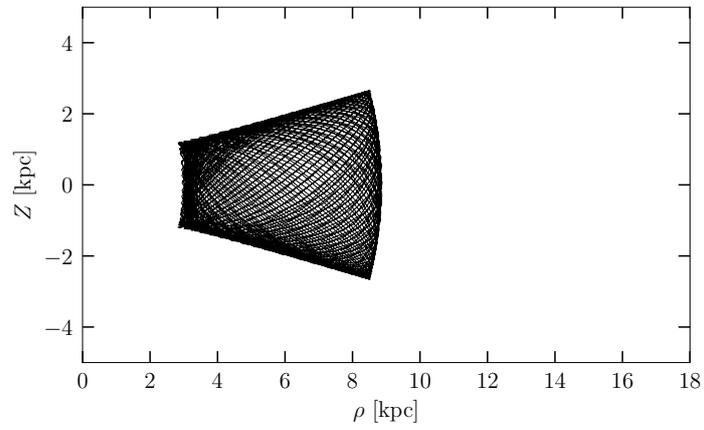
Figure 15: Thick-disk orbit of HE 0452-3444.
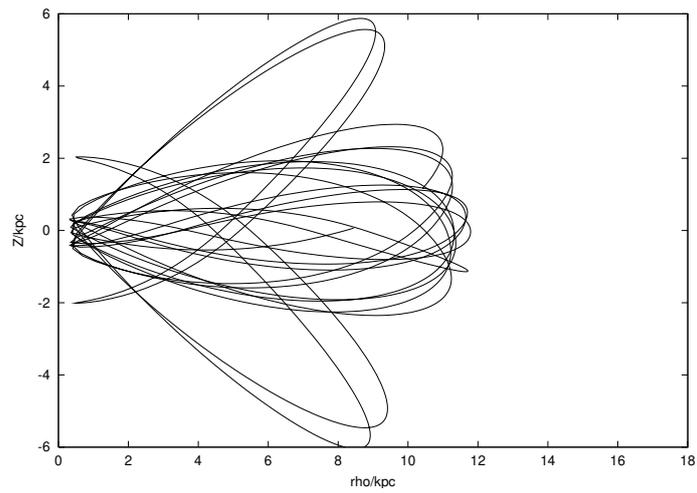
Figure 16: (Chaotic) halo orbit of HS 1527+0614 from Pauli et al. (2006).

18

5. Kinematic analysis

The orbits and kinematic parameters of the stars were calculated with the PYTHON package GALPY, designed for the study of galactic dynamics (Bovy 2015). Stellar orbits in a given Galactic potential are obtained from the integration of the equations of motion. The standard *MWPotential2014* has an exponentially cut-off power-law bulge, a exponential disk and a power-law halo (Bovy 2015, and references therein), whereas Pauli et al. (2006) used a different Galactic potential from Allen & Santillan (1991). The kinematic paramaters needed for the classification of the stars are derived from the orbit integration. The input parameters for the orbit integration (right ascension, declination, parallax, proper motion components, radial velocity, rotational velocity of the Galaxy at the position of the Sun (V_0), solar distance to the Galactic center (R_0), and Solar motion), correspond to the initial conditions of each star. For the solar parameters, I used the values $v_0 = (220 \pm 9)\,\mathrm{km/s}$, $r_0 = (8.00 \pm 0.29)\,\mathrm{kpc}$ and $(U_\odot, V_\odot, W_\odot) = (10.00 \pm 0.36,\ 5.25 \pm 0.62,\ 7.17 \pm 0.38)\,\mathrm{km/s}$ (Dehnen & Binney 1998). Pauli used the same values, except for $R_0 = 8.5\,\mathrm{kpc}$, but neglected the errors on these parameters.

In order to propagate the uncertainties on the input parameters, a Monte Carlo simulation was performed.

5.1. Montecarlo simulation

For an input parameter, x_0, with uncertainty, σ, the uncertainty of the output $f(x)$ can be obtained as follows: a large number of random x-values, obeying a Gaussian distribution, with x_0 as its mean value and σ as its standard deviation, is generated. Then $f(x)$ is computed for all these x-values and the mean value and uncertainty of f is calculated.

Analogously, the uncertainty of an output $g(x, y)$ with inputs $x \pm \sigma_x$ and $y \pm \sigma_y$ can be calculated by generating a large number of pairs of random x- and y-values and computing g for all those pairs. The same can be done for any number of input parametes.

Therefore the input parameters for the case of this sample were variied based on their uncertainties and $10\,000$ sets of input values were generated per star. As the correlations between α, δ, μ_α, μ_δ and ϖ, given by *Gaia*, could be used, the $10\,000$ sets of input values proved to have a good balance between the necessary computation time and the sampling of the output values.

The code was run on the cluster of the Dr. Karl Remeis Observatory, where one core per star was used to integrate the $10\,000$ orbits. On average, it took about two hours to compute all orbits for one star, and the computation for the whole sample was finished within one day. For each orbit, the galactocentric velocity components U, V and W, and the orbital angular momentum in Z-direction, J_Z and the orbital eccentricity, e, were computed. Finally, their mean values and standard deviations were computed for each star.

5.2. Results

In Figure 17, the velocity component U is plotted versus the velocity component V for the sample of 609 white dwarfs. The error bars indicate the 1σ uncertainties. The majority of

the white dwarfs are located inside the $3\sigma_{\text{thin}}$-limit, whereas only seven stars are outside the $3\sigma_{\text{thick}}$-limit and therefore are considered halo candidates. The two stars on the very left of Figure 17, WD 1524−749 and WD 1448+077, have $V < 0$, which indicates that they move against the Galactic rotation. This behaviour strongly favours a halo membership.
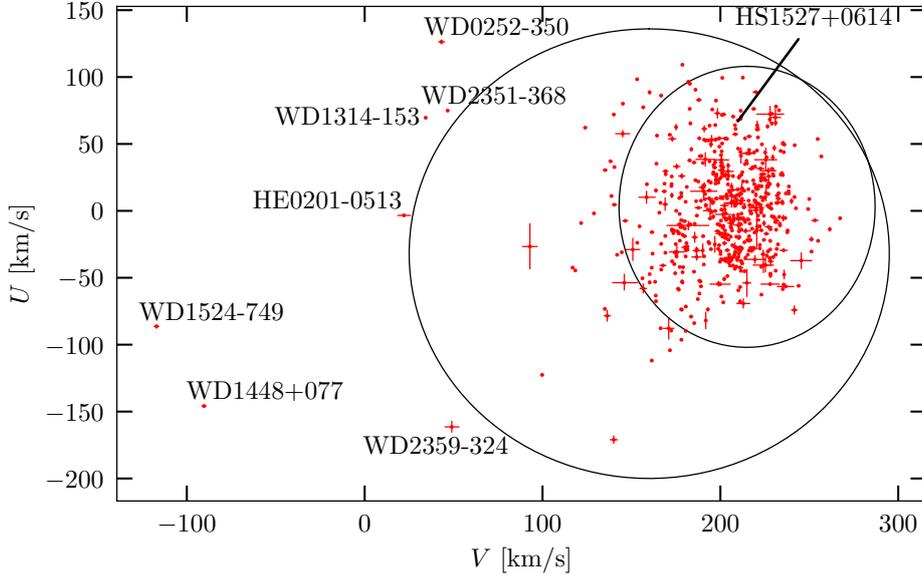
Figure 17: $U - V$-diagram of the white dwarfs with $3\sigma_{\text{thin}}$ and $3\sigma_{\text{thick}}$ contours.
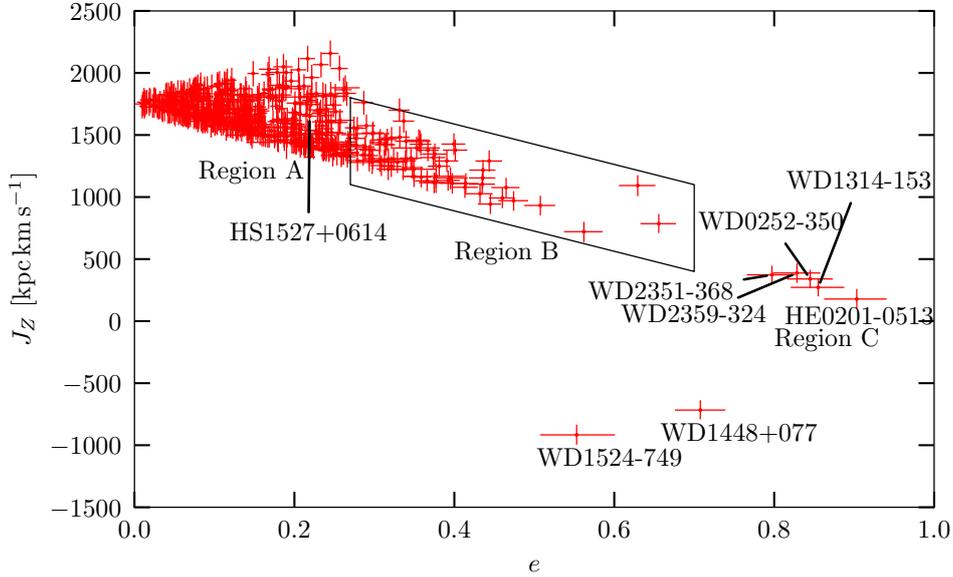
Figure 18: $J_Z - e$-diagram of the white dwarfs.

The Z-component of the angular momentum, J_Z, of the white dwarfs' orbits is plotted versus the eccentricity e of the orbit in Figure 18. The error bars indicate the 1σ uncertainties.

Again, most white dwarfs are located in region A, where the majority of thin-disk members are expected to be situated. WD 1524−749 and WD 1448+077 have negative values of J_Z (see Figure 18) because they move on retrograde orbits, as discussed above.

The positions of HS 1527+0614 in the $U − V$- and $J_Z − e$-diagrams suggest that this white dwarf belongs to the thin-disk population, as it lies inside the $3\sigma_{\text{thin}}$-contour in Figure 17 and inside Region A in Figure 18. Pauli et al. (2006), however, classified it as a halo star. The reason for this classification change is presumably the discrepancy of the measured proper motions, mentioned in Section 3.

In Figure 18 Region B seems like an extension of Region A towards higher eccentricities and lower angular momenta. One might ask why such an extension is not observed towards higher angular momenta. A possible reason for this observation is the bias of the white dwarf sample, as it only contains stars below $\delta = 25.3°$. Thus no stars of the sample are located in the northern half of the 2nd Galactic quadrant ($90° \leq l \leq 180°$, $b \geq 0°$), as can be seen in Figure 19. It is imaginable that some stars located in this quadrant might have orbits of higher angular momenta compared to Region B. This could result in an extension of Region A in both directions.
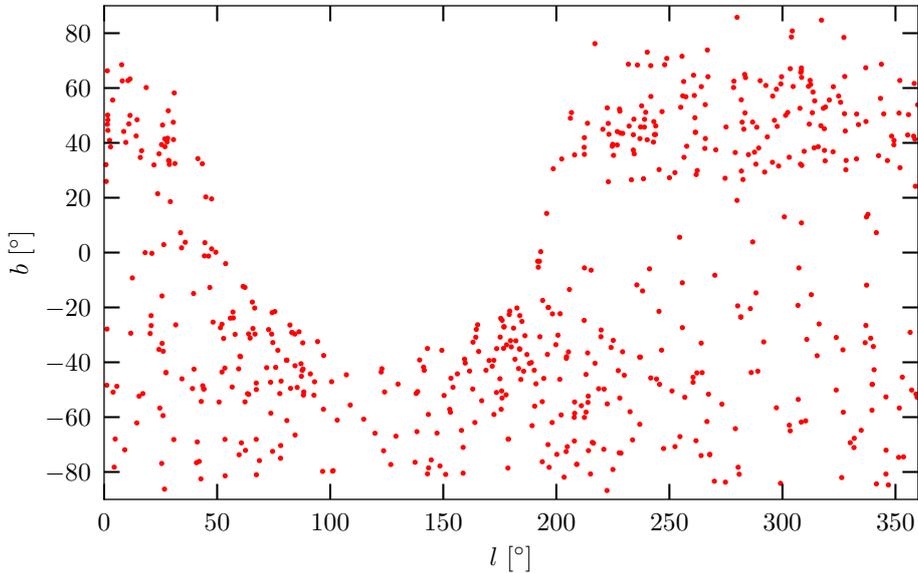
Figure 19: Distribution of the positions of the 609 white dwarfs in Galactic coordinates l and b.

As all seven halo candidates (labeled with their names in Figure 17 and 18) are outside of the $3\sigma_{\text{thick}}$-contours in the $U − V$-diagram and in Region C in the $J_Z − e$-diagram, they are – according to the classification scheme, presented in Section 4 – all part of the halo population, regardless of the shape of their orbits. Nevertheless, the shapes of the orbits, that can be seen in Figure 20, have been analysed and the respective classification values for the halo candidates can be seen in Table 4. None of the orbits of the halo stars is chaotic, instead they are all similar to thick-disk-like orbits with high eccentricities.

21
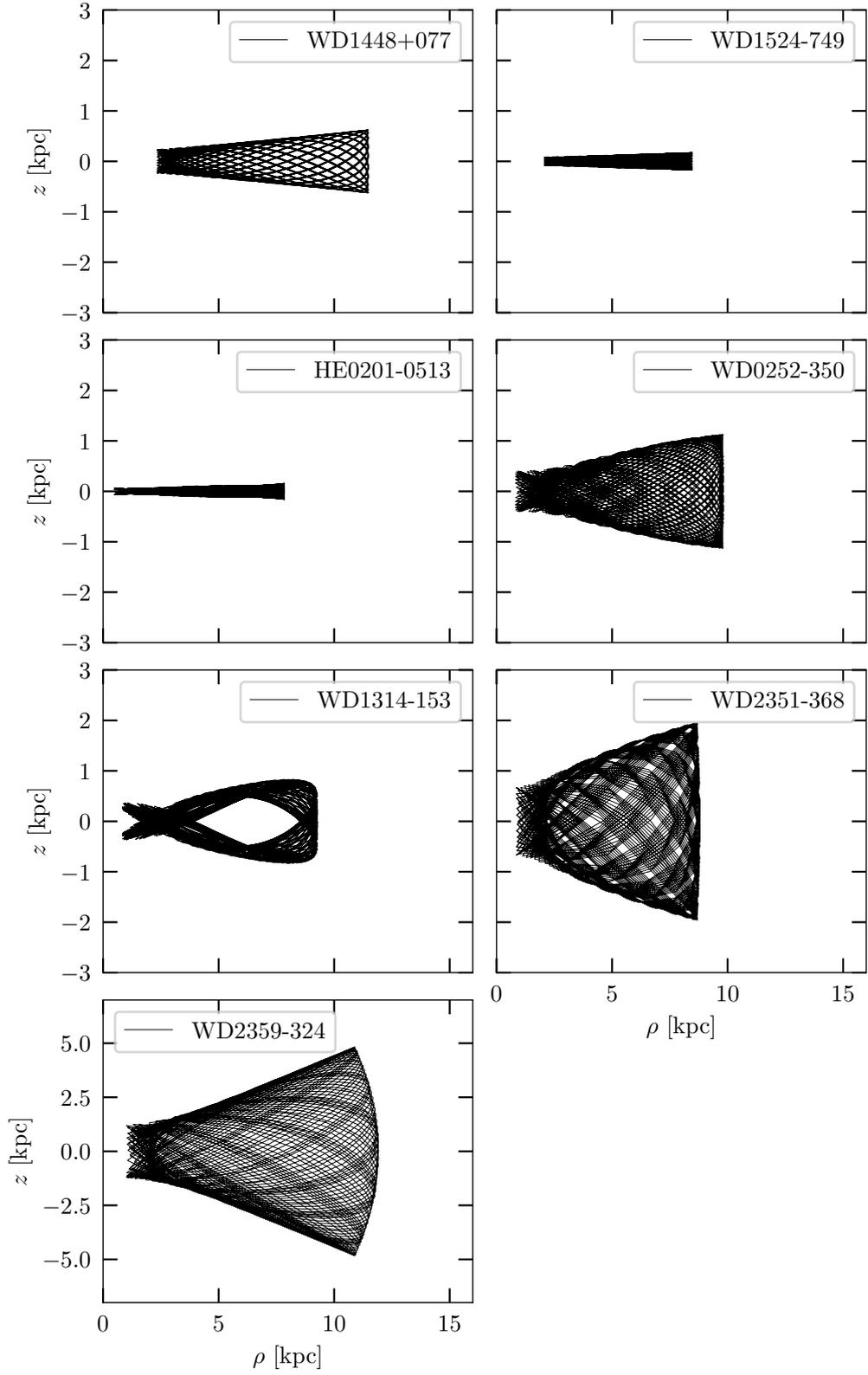
Figure 20: Orbits of the halo stars. WD 1448+077 and WD 1524−749 move against the Galactic rotation.

The classification values for the thick disk candidates are listed in Table 5. In Table 6 the stars, for which the classification has changed with respect to Pauli et al. (2006) due to *Gaia* DR2 astrometry, are listed. One of them is the previously mentioned HS 1527+0614, which has changed from a halo star to a thin-disk star. There are also six stars for which the classification has changed from thick disk to thin disk, and for eight stars the other way round.

5.3. The final break-down

Out of the 609 white dwarfs in the sample, 7 stars have been classified as halo members (1 %), 41 as thick-disk members (7 %) and the remaining 561 as thin-disk members (92 %). This distribution of the three memberships is visualized in Figure 21.
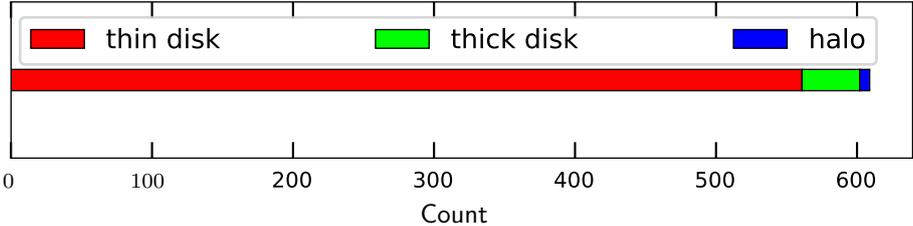
Figure 21: Distribution of the sample into thin-disk (561), thick-disk (41) and halo stars (7).

6. Summary and Outlook

White dwarfs are an old population of stars, as they are the final state of the evolution of low mass stars ($M < 10\,M_\odot$). Thus, they exist in all populations of the Milky Way: thin and thick disk and the Galactic halo. The best studied sample of white dwarfs originates from the ESO Supernova Ia Progenitor Survey (SPY).

Pauli et al. (2006) already analyzed the kinematics of 398 DA white dwarfs from SPY from spectroscopic distances, ground-based proper motions and high-precision radial velocities. Recently, the *Gaia* mission provided for the first time trigonometric parallaxes and proper motions. A comparison shows that they are in agreement with the spectroscopic distances and ground-based proper motions used by Pauli et al. (2006), but are 100 times more precise than the ground-based values. Therefore, it is tempting to revisit the SPY sample of DA white dwarfs for an improved kinematic analysis.

The sample to be studied is extended to 609 of the 650 white dwarfs of the SPY sample, discarding 31 binaries, 3 without *Gaia* measurements, 2 subdwarfs and 5 with atmospheric parameters outside the model grid.

The PYTHON package GALPY is used to calculate the Galactic orbits and kinematic parameters of the white dwarfs. Errors on the astrometric input parameters, obtained form *Gaia* DR2, are propagated using a Monte Carlo simulation.

Depending on the positions in the $U-V$- and J_Z-e-diagrams and on the shape of the Galactic orbits, the white dwarfs' population membership to the thin disk, thick disk and Galactic halo is determined, using the classification scheme developed by Pauli et al. (2006). 7 halo ($1\,\%$), 41 thick-disk ($7\,\%$) and 561 thin-disk ($92\,\%$) stars are identified.

Although this is the so-far largest sample of white dwarfs analyzed, using full six parameter astrometry, yet, it would be crucial to expand the investigated sample to a size of a few to several thousand white dwarfs, distributed homogeneously over the entire sky. Not only could the statistics be increased, but by including stars from the Northern part of the second Galactic quadrant in the analysis also a possible extension of Region A in the $J_Z - e$-diagram towards higher angular momenta could be observed. Such large samples of spectroscopically confirmed white dwarfs will be obtained in the next ten years, thanks to the new generation of multi-fibre spectroscopic surveys, such as *WEAVE* (first light in 2020; Dalton et al. 2014), *DESI* (first light in 2019; DESI Collaboration et al. 2016), and *4MOST* (first light in 2022; de Jong et al. 2014), leading to the first statistically-significant volume-complete samples of white dwarfs for the study of stellar dynamics in the vicinity of the Sun.

Appendices

A. A comment on tangential velocities

In most kinematic studies of large samples, no radial velocities are available. Often, limits on the trangential velocities are used to characterize the stellar populations. Gaia Collaboration et al. (2018a), for example, use $v_t \leq 40\,\mathrm{km/s}$ for thin-disk stars, $60\,\mathrm{km/s} \leq v_t \leq 150\,\mathrm{km/s}$ for thick-disk stars and $v_t \geq 200\,\mathrm{km/s}$ for halo stars.
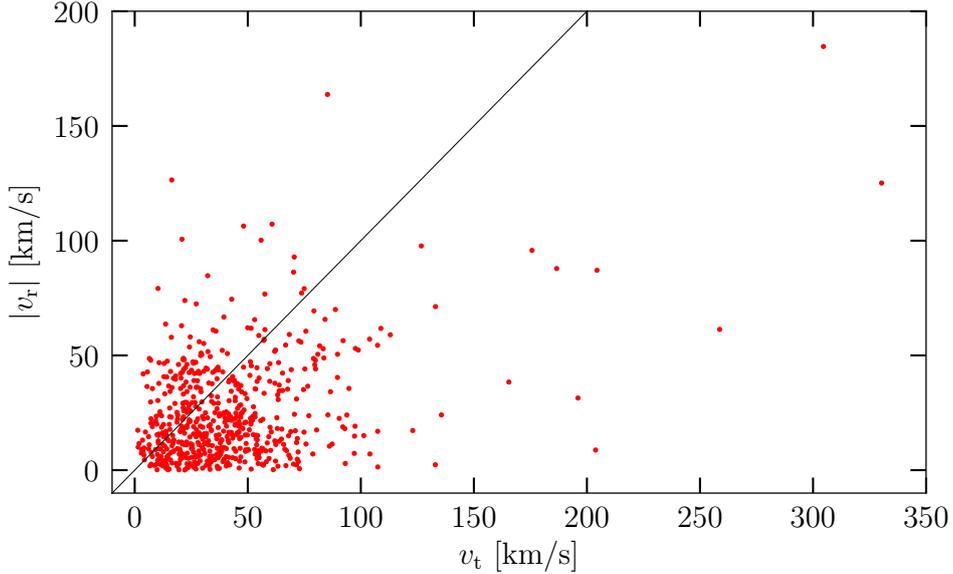
Figure 22: Radial velocities v_r versus tangential velocities v_t of the 609 white dwarfs.

The tangential velocities of the 609 white dwarfs are plotted versus their radial velocities in Figure 22. For about two thirds of the stars, the 3D space motion is dominated by the tangential velocity. The seven halo white dwarfs have tangential velocities $v_t \geq 186\,\mathrm{km/s}$, only two of them have $v_t \leq 200\,\mathrm{km/s}$. All of the halo white dwarfs are dominated by their tangential velocity. Only two thick-disk white dwarfs have $v_t \geq 150\,\mathrm{km/s}$ and only four have $v_t \leq 60\,\mathrm{km/s}$. The remaining 35 thick-disk members have tangential velocities within the respective limit of Gaia Collaboration et al. (2018a). Ten of the 41 thick-disk members are dominated by their radial velocities. However, there are more than 50 thin-disk members exceeding the limit of $v_t = 40\,\mathrm{km/s}$. Thus, the distribution of the tangential velocities of the white dwarf sample supports the lower tangential-velocity-limit of the halo, and the upper limit of the thick disk given by Gaia Collaboration et al. (2018a). But the distinction between thin and thick disk seems to be a rather continuous transition, instead.

B. List of tables

Table 4: Classification values for the halo candidates.

star	c_{UV}	c_{J_Z-e}	c_{orb}	c	classification
HE 0201−0513	+1	+1	−1	+1	halo
WD 0252−350	+1	+1	−1	+1	halo
WD 1314−153	+1	+1	−1	+1	halo
WD 1448+077	+1	+1	+1	+3	halo
WD 1524−749	+1	+1	+1	+3	halo
WD 2351−368	+1	+1	−1	+1	halo
WD 2359−324	+1	+1	−1	+1	halo

Table 5: Classification values for the thick-disk candidates.

star	c_{UV}	c_{J_Z-e}	c_{orb}	c	classification
HE0150+0045	−1	+1	−1	−1	*thin disk*
HE0245−0008	−1	+1	−1	−1	*thin disk*
HE0336−0741	−1	+1	−1	−1	*thin disk*
HE0414−4039	−1	+1	−1	−1	*thin disk*
HE0452−3444	+1	+1	+1	+3	thick disk
HE0508−2343	+1	+1	−1	+1	thick disk
HE1124+0144	+1	+1	−1	+1	thick disk
HE1215+0227	+1	+1	−1	+1	thick disk
HS0213+1145	−1	+1	−1	−1	*thin disk*
HS0223+1211	−1	+1	−1	−1	*thin disk*
HS0820+2503	+1	+1	+1	+3	thick disk
HS0949+0823	+1	+1	+1	+3	thick disk
HS1338+0807	+1	+1	−1	+1	thick disk
HS1432+1441	+1	+1	−1	+1	thick disk
MCT0105−1634	−1	+1	−1	−1	*thin disk*
WD0005−163	−1	+1	−1	−1	*thin disk*
WD0011+000	−1	+1	−1	−1	*thin disk*
WD0024−556	−1	+1	−1	−1	*thin disk*
WD0032−175	−1	+1	−1	−1	*thin disk*
WD0102−185	−1	+1	−1	−1	*thin disk*
WD0103−278	−1	+1	−1	−1	*thin disk*
WD0124−257	+1	+1	−1	+1	thick disk
WD0127−050	−1	+1	−1	−1	*thin disk*
WD0133−116	−1	+1	+1	+1	thick disk
WD0138−236	−1	+1	+1	+1	thick disk
WD0151+017	−1	+1	−1	−1	*thin disk*
WD0204−233	+1	+1	+1	+3	thick disk

WD0205−304	−1	+1	−1	−1	*thin disk*
WD0255−705	+1	+1	−1	+1	thick disk
WD0257+080	−1	+1	−1	−1	*thin disk*
WD0302+027	−1	+1	+1	+1	thick disk
WD0326−273	+1	+1	−1	+1	thick disk
WD0336+040	−1	+1	−1	−1	*thin disk*
WD0352+018	−1	+1	−1	−1	*thin disk*
WD0352+052	+1	+1	+1	+3	thick disk
WD0440−038	+1	+1	+1	+3	thick disk
WD0548+000	−1	+1	−1	−1	*thin disk*
WD0628−020	−1	+1	−1	−1	*thin disk*
WD0732−427	+1	+1	+1	+3	thick disk
WD0752−676	−1	+1	−1	−1	*thin disk*
WD0928−713	−1	+1	−1	−1	*thin disk*
WD0955+247	−1	+1	−1	−1	*thin disk*
WD0956+045	+1	+1	−1	+1	thick disk
WD1010+043	−1	+1	−1	−1	*thin disk*
WD1013−010	+1	+1	−1	+1	thick disk
WD1105−048	−1	+1	−1	−1	*thin disk*
WD1126−222	−1	+1	−1	−1	*thin disk*
WD1147+255	−1	+1	−1	−1	*thin disk*
WD1152−287	−1	+1	−1	−1	*thin disk*
WD1254+223	−1	+1	−1	−1	*thin disk*
WD1257+037	+1	+1	−1	+1	thick disk
WD1308−301	−1	+1	−1	−1	*thin disk*
WD1323−514	+1	+1	−1	+1	thick disk
WD1327−083	+1	+1	−1	+1	thick disk
WD1330+036	−1	+1	−1	−1	*thin disk*
WD1334−678	+1	+1	−1	+1	thick disk
WD1344+106	−1	+1	−1	−1	*thin disk*
WD1410+168	+1	+1	+1	+3	thick disk
WD1418−088	−1	+1	−1	−1	*thin disk*
WD1426−276	+1	+1	+1	+3	thick disk
WD1434−223	−1	+1	−1	−1	*thin disk*
WD1451+006	−1	+1	−1	−1	*thin disk*
WD1507+021	−1	+1	−1	−1	*thin disk*
WD1531+184	−1	+1	−1	−1	*thin disk*
WD1547+015	+1	+1	+1	+3	thick disk
WD1609+135	−1	+1	+1	+1	thick disk
WD1614−128	+1	+1	−1	+1	thick disk
WD1625+093	−1	+1	−1	−1	*thin disk*
WD1636+057	+1	+1	+1	+3	thick disk
WD1716+020	+1	+1	−1	+1	thick disk
WD1736+052	−1	+1	−1	−1	*thin disk*

WD1821−131	+1	+1	−1	+1	thick disk
WD1824+040	−1	+1	−1	−1	*thin disk*
WD1834−781	+1	+1	+1	+3	thick disk
WD1918+110	−1	+1	+1	+1	thick disk
WD1932−136	−1	+1	−1	−1	*thin disk*
WD1950−432	−1	+1	+1	+1	thick disk
WD1952−206	+1	+1	+1	+3	thick disk
WD2029+183	+1	+1	−1	+1	thick disk
WD2058+181	−1	+1	−1	−1	*thin disk*
WD2120+054	+1	+1	−1	+1	thick disk
WD2136+229	−1	+1	−1	−1	*thin disk*
WD2159−414	−1	+1	+1	+1	thick disk
WD2159−754	+1	+1	−1	+1	thick disk
WD2235+082	−1	+1	−1	−1	*thin disk*
WD2240−045	+1	+1	−1	+1	thick disk
WD2253+054	−1	+1	−1	−1	*thin disk*
WD2318+126	−1	+1	−1	−1	*thin disk*
WD2322−181	−1	+1	−1	−1	*thin disk*
WD2333−049	−1	+1	−1	−1	*thin disk*
WD2347+128	−1	+1	−1	−1	*thin disk*
WD2353+026	−1	+1	−1	−1	*thin disk*

Table 6: Classification changes due to *Gaia* DR2 astrometry.

star	Pauli et al. 2006	Gaia DR2
HS 1527+0614	halo	thin disk
HE 0409−5154	thick disk	thin disk
HE 0416−1034	thick disk	thin disk
WD 1152−287	thick disk	thin disk
WD 1507+021	thick disk	thin disk
WD 2322−181	thick disk	thin disk
WD 2350−083	thick disk	thin disk
HE 1215+0227	thin disk	thick disk
WD 0124−257	thin disk	thick disk
WD 0138−236	thin disk	thick disk
WD 0302+027	thin disk	thick disk
WD 0956+045	thin disk	thick disk
WD 1609+135	thin disk	thick disk
WD 1636+057	thin disk	thick disk
WD 1918+110	thin disk	thick disk

Table 7: Kinematic parameters of the 609 white dwarfs.

star	U	V	W	J_Z	e
EC12489−2750	−0.75	−31.55	−9.18	1505.96	0.15
EC13123−2523	−39.75	−38.73	7.82	1458.54	0.18
HE0031−5525	13.07	−27.86	−29.96	1575.43	0.13
HE0032−2744	−1.27	−34.01	−30.29	1526.58	0.14
HE0043−0318	−2.09	−1.41	−52.73	1791.15	0.05
HE0049−0940	−31.74	−10.08	−8.63	1723.08	0.08
HE0103−3253	−38.85	2.75	−17.74	1822.9	0.11
HE0106−3253	−3.09	−13.62	−24.07	1692.47	0.05
HE0130−2721	7.88	−44.13	−1.99	1449.36	0.2
HE0138−4014	30.89	−36.69	−12.91	1505.16	0.21
HE0145−0610	−40.09	−14.06	−34.12	1692.17	0.11
HE0150+0045	55.39	−42.1	−22.33	1473.2	0.28
HE0152−5009	−9.9	−8.57	−37.39	1730.53	0.01
HE0201−0513	−13.4	−203.19	−13.07	178.22	0.9
HE0204−3821	−17.29	−24.9	−5.33	1605.09	0.1
HE0204−4213	58.24	2.52	−0.38	1817.91	0.24
HE0210−2012	−38.43	6.41	−3.38	1861.23	0.11
HE0211−2824	11.92	−37.69	−25.55	1501.57	0.18
HE0219−4049	−17.06	−17.71	−9.12	1661.24	0.07
HE0221−0535	−3.13	9.46	−15.43	1890.42	0.08
HE0221−2642	11.16	−30.64	−23.2	1564.74	0.14
HE0222−2336	16.01	−18.19	0.5	1671.39	0.11
HE0222−2630	−31.83	−8.32	−24.99	1741.21	0.07
HE0245−0008	−63.49	−65.02	−13.9	1291.76	0.34
HE0246−5449	−18.3	−11.34	−3.03	1707.42	0.04
HE0255−1100	35.12	−4.68	11.55	1780.84	0.16
HE0256−1802	60.37	−13.57	−33.34	1709.7	0.24
HE0257−2104	39.72	−1.91	−37.47	1796.34	0.17
HE0300−2313	−5.63	−8.89	−7.28	1736.59	0.02
HE0303−2041	2.24	−21.76	−26.92	1631.41	0.09
HE0305−1145	−28.91	−45.39	−3.15	1455.15	0.21
HE0308−2305	7.24	−5.34	−7.75	1761.82	0.06
HE0317−2120	−16.81	−22.01	−22.73	1629.52	0.09
HE0320−1917	−30.46	−21.92	−26.27	1638.12	0.1
HE0324−0646	−5.59	−33.41	−10.82	1541.81	0.14
HE0324−2234	−42.74	5.85	−13.9	1860.52	0.12
HE0330−4736	−14.43	4.78	−23.43	1842.47	0.05
HE0333−2201	12.68	−2.41	−22.57	1786.56	0.08
HE0336−0741	−21.6	−70.73	−27.86	1247.07	0.32
HE0338−3025	34.03	−13.99	−15.27	1693.51	0.16
HE0344−1207	−14.35	−29.26	6.63	1573.63	0.12

HE0348−2404	−16.28	−9.74	−10.93	1733.11	0.03
HE0348−4445	−16.78	−4.0	−18.29	1775.75	0.02
HE0349−2537	16.2	4.62	0.78	1846.33	0.11
HE0358−5127	−9.22	−2.21	−12.53	1786.71	0.02
HE0403−4129	−0.85	7.36	−13.38	1868.12	0.08
HE0404−1852	−21.63	−19.45	−2.43	1659.81	0.08
HE0409−5154	42.54	−33.54	−37.35	1531.56	0.23
HE0414−4039	4.56	−56.81	−7.21	1349.83	0.26
HE0416−1034	−45.05	−20.32	−5.62	1655.24	0.14
HE0416−3852	−40.82	−16.82	0.36	1676.19	0.11
HE0417−3033	−49.8	−51.13	19.17	1406.47	0.25
HE0418−1021	−19.73	−13.91	−7.83	1700.92	0.05
HE0418−5326	−17.1	27.9	−5.8	2029.93	0.17
HE0423−2822	−44.46	−38.54	−22.23	1503.64	0.2
HE0425−2015	−6.77	−11.72	−16.97	1724.05	0.03
HE0426−0455	0.33	16.4	−0.77	1937.99	0.12
HE0426−1011	−40.7	−50.66	−6.15	1406.49	0.25
HE0436−1633	34.45	−24.49	−18.65	1613.65	0.18
HE0452−3429	−20.92	−25.26	−26.42	1605.26	0.1
HE0452−3444	52.17	−101.28	68.6	992.33	0.46
HE0456−2347	13.52	−26.05	−14.55	1609.74	0.14
HE0507−1855	−3.9	−5.03	−7.01	1774.26	0.03
HE0508−2343	−97.74	−58.86	−11.97	1346.02	0.38
HE0516−1804	3.0	−13.99	−4.47	1699.72	0.07
HE0532−5605	−7.67	−37.61	−19.83	1501.07	0.16
HE1012−0049	3.17	7.55	−3.02	1868.86	0.08
HE1053−0914	5.61	−18.5	−7.96	1655.47	0.09
HE1124+0144	−99.72	−44.73	23.85	1449.81	0.34
HE1152−1244	−4.24	−16.06	1.74	1670.56	0.06
HE1215+0227	−63.68	−79.29	−13.83	1167.66	0.38
HE1225+0038	−14.46	7.96	2.9	1863.44	0.07
HE1233−0519	12.96	0.08	−5.68	1796.23	0.09
HE1247−1130	2.41	−14.36	−18.11	1676.44	0.07
HE1252−0202	11.09	−26.42	−13.4	1581.87	0.13
HE1258+0123	14.53	−0.52	22.44	1791.03	0.09
HE1307−0059	25.49	−10.29	15.14	1709.67	0.12
HE1310−0337	−20.01	−48.15	11.48	1406.29	0.21
HE1315−1105	−15.05	−22.8	17.59	1614.46	0.08
HE1325−0854	−4.66	3.3	−22.82	1821.26	0.05
HE1326−0041	23.84	−20.81	−11.52	1623.1	0.14
HE1328−0535	−40.7	−49.74	−16.55	1382.28	0.24
HE1335−0332	−30.12	−14.88	3.12	1673.46	0.08
HE1340−0530	7.54	−35.47	−21.4	1492.06	0.16
HE1413+0021	2.98	13.18	−3.8	1892.92	0.1

HE1429−0343	53.08	1.27	9.77	1801.3	0.22
HE1441−0047	−2.69	14.74	−8.03	1907.94	0.1
HE1511−0448	−15.07	4.91	−36.27	1789.99	0.06
HE1518−0020	8.59	−52.82	5.74	1369.92	0.24
HE1518−0344	9.03	−34.3	−8.64	1498.96	0.16
HE1522−0410	8.44	−2.09	7.92	1772.01	0.06
HE2133−1332	−15.72	−15.76	−24.71	1673.59	0.05
HE2135−4055	40.82	10.01	−14.91	1874.75	0.19
HE2140−1825	0.13	−17.29	9.51	1654.6	0.07
HE2148−3857	29.81	4.24	4.13	1808.56	0.14
HE2155−3150	10.04	−6.19	−5.12	1735.83	0.07
HE2159−1649	−18.31	5.63	−26.87	1831.46	0.07
HE2203−0101	6.26	−4.89	−4.19	1754.39	0.05
HE2205−1355	−9.51	−5.35	−6.34	1750.38	0.01
HE2218−2706	−51.84	−2.22	35.42	1776.67	0.15
HE2220−0633	55.28	3.71	1.58	1825.99	0.22
HE2221−1630	24.93	−11.38	−28.79	1705.58	0.12
HE2230−1230	−44.57	4.47	−7.49	1821.76	0.13
HE2231−2647	−33.44	−11.72	20.54	1699.55	0.08
HE2238−0433	−21.94	1.86	−13.71	1804.7	0.06
HE2246−0658	15.83	1.97	−26.79	1808.71	0.09
HE2251−6218	−19.48	−8.72	−10.39	1723.25	0.03
HE2315−0511	44.27	−25.9	−15.96	1594.57	0.2
HE2334−1355	17.53	−29.27	−17.56	1563.2	0.14
HE2347−4608	43.16	−34.38	−19.72	1513.13	0.23
HE2356−4513	25.65	−1.5	−22.43	1782.96	0.12
HS0002+1635	−38.65	−30.57	−6.4	1561.75	0.16
HS0047+1903	−4.39	−13.77	−12.16	1696.72	0.04
HS0051+1145	−39.4	−21.37	−17.2	1637.92	0.13
HS0129+1041	−50.91	−19.84	−22.5	1650.68	0.16
HS0130+0156	−20.55	−15.11	−12.38	1704.03	0.07
HS0145+1737	−16.75	−19.56	3.55	1655.45	0.08
HS0146+1847	−24.73	−51.4	−0.13	1392.71	0.23
HS0200+2449	−24.68	12.55	−12.84	1916.18	0.11
HS0213+1145	−83.7	−32.31	−19.93	1554.46	0.28
HS0223+1211	62.9	−26.91	16.39	1618.28	0.26
HS0225+0010	−0.98	−13.07	−9.38	1704.66	0.05
HS0241+1411	9.31	7.11	3.1	1875.62	0.09
HS0307+0746	23.07	−5.7	−27.93	1767.37	0.11
HS0309+1001	−55.13	−11.68	−52.79	1725.9	0.16
HS0315+0858	−31.6	−20.69	−0.33	1649.22	0.11
HS0325+2142	−46.18	−24.9	−22.75	1611.54	0.16
HS0329+1121	9.12	1.82	12.84	1836.79	0.08
HS0331+2240	−15.54	42.07	19.93	2157.54	0.24

HS0337+0939	−43.51	0.9	−22.67	1825.96	0.12
HS0344+0944	2.05	−5.29	−17.91	1776.94	0.04
HS0345+1324	−15.43	10.06	−19.06	1903.87	0.08
HS0346+0755	−19.28	−0.72	−25.57	1823.54	0.04
HS0400+1451	−47.5	−19.5	−4.07	1652.06	0.14
HS0401+1454	15.68	−27.65	−8.46	1591.44	0.14
HS0412+0632	−6.2	−33.39	−8.65	1542.21	0.14
HS0424+0141	−63.83	−10.32	−14.64	1806.03	0.18
HS0503+0154	20.4	−24.69	−15.9	1637.26	0.14
HS0507+0434A	−0.63	−21.41	−14.27	1638.87	0.09
HS0507+0434B	−9.07	−24.66	−17.99	1611.95	0.1
HS0820+2503	−88.43	−88.87	−114.61	1116.54	0.38
HS0926+0828	−47.53	−22.22	−16.1	1637.72	0.15
HS0929+0839	−42.9	−17.28	−20.37	1678.96	0.12
HS0931+0712	28.49	−33.71	7.98	1548.48	0.2
HS0933+0028	−7.81	−5.0	−7.23	1781.48	0.02
HS0937+0130	0.28	−0.27	−9.77	1808.9	0.05
HS0940+1129	−31.67	−0.77	43.02	1807.2	0.09
HS0943+1401	−8.41	3.39	−3.95	1837.06	0.05
HS0944+1913	−42.22	−25.16	12.17	1604.84	0.14
HS0949+0823	−5.41	−84.89	−60.32	1130.61	0.37
HS0949+0935	−34.18	−22.92	−17.66	1639.0	0.11
HS1003+0726	−2.42	−36.14	29.52	1516.85	0.15
HS1013+0321	12.88	−39.25	−0.35	1490.79	0.19
HS1043+0258	−14.09	3.66	−1.98	1835.36	0.05
HS1053+0844	−19.27	−18.52	−11.75	1660.29	0.07
HS1102+0032	−46.37	−23.9	2.44	1612.45	0.15
HS1115+0321	−32.31	−9.23	7.93	1730.99	0.07
HS1136+0326	−23.73	2.9	−1.93	1824.2	0.06
HS1136+1359	−52.43	−14.11	−22.07	1696.12	0.14
HS1144+1517	−60.91	−23.09	−1.88	1621.68	0.19
HS1153+1416	−11.01	−30.23	−23.23	1559.43	0.12
HS1204+0159	5.29	−31.5	−12.24	1543.71	0.14
HS1243+0132	−11.73	−22.27	19.26	1616.34	0.08
HS1249+0426	2.65	1.63	7.12	1809.2	0.06
HS1305+0029	−25.21	−49.47	4.69	1398.83	0.22
HS1308+1646	−0.58	−23.9	23.76	1608.63	0.09
HS1338+0807	76.19	−58.55	19.88	1318.02	0.37
HS1410+0809	8.42	1.27	10.42	1804.18	0.07
HS1430+1339	−7.42	−12.09	1.98	1699.42	0.04
HS1432+1441	86.54	−43.25	19.73	1448.02	0.36
HS1447+0454	−29.36	−14.65	−9.79	1675.19	0.08
HS1517+0814	52.04	−4.36	−9.85	1752.73	0.21
HS1527+0614	54.0	−17.04	12.1	1651.67	0.22

HS1609+1426	−54.85	−13.64	3.68	1676.81	0.16
HS1614+1136	−8.95	−22.83	4.26	1606.5	0.09
HS1616+0247	−15.43	−17.71	−2.78	1640.58	0.07
HS1641+1124	14.99	−14.83	11.35	1670.31	0.09
HS1646+1059	26.29	−28.22	−31.64	1557.85	0.16
HS1648+1300	−38.01	−3.07	−37.22	1759.08	0.1
HS1705+2228	−32.26	−48.04	−29.86	1409.2	0.22
HS2046+0044	−38.09	−6.28	1.04	1719.83	0.11
HS2056+0721	−24.45	−2.31	−11.86	1771.04	0.06
HS2058+0823	−25.0	−11.04	5.76	1696.98	0.07
HS2059+0208	−27.1	0.61	3.43	1786.05	0.07
HS2108+1734	−4.95	−3.57	−1.25	1764.98	0.01
HS2130+1215	1.04	−21.81	2.85	1609.98	0.09
HS2132+0941	17.16	−27.41	15.28	1577.09	0.14
HS2138+0910	−3.2	−44.78	−3.12	1438.72	0.2
HS2148+1631	−28.91	−34.93	−43.2	1511.3	0.16
HS2210+2323	−7.42	2.49	−10.51	1818.63	0.04
HS2220+2146A	−2.83	−17.9	−20.6	1656.19	0.07
HS2220+2146B	−3.32	−18.58	−20.56	1652.58	0.07
HS2225+2158	45.64	−9.04	−0.03	1732.06	0.18
HS2229+2335	−38.64	−44.17	−6.32	1443.7	0.22
HS2233+0008	30.01	0.8	−5.08	1804.12	0.14
HS2240+1234A	33.12	−8.91	−19.51	1729.38	0.14
HS2240+1234B	33.01	−10.2	−18.78	1720.85	0.14
HS2244+0305	−20.93	−43.26	22.06	1440.65	0.19
HS2244+2103	21.5	−7.82	−16.25	1742.76	0.09
HS2259+1419	−10.12	−28.16	39.62	1573.04	0.1
MCT0031−3107	51.34	−34.34	8.97	1519.86	0.25
MCT0033−3440	−37.42	−14.56	−16.24	1683.19	0.1
MCT0105−1634	19.64	−56.13	−4.78	1360.27	0.27
MCT0110−1617	−25.89	12.32	−23.87	1914.11	0.11
MCT0111−3806	9.83	−20.99	−12.93	1628.01	0.1
MCT0138−4014	30.92	−35.9	−10.26	1511.37	0.21
MCT2343−1740	−4.12	6.37	−1.53	1845.76	0.06
MCT2345−3940	−44.58	−17.83	8.56	1650.92	0.13
MCT2349−3627	−5.07	−56.32	9.79	1335.15	0.25
MCT2352−1249	43.18	−30.15	26.16	1559.61	0.2
WD J0148−255	−26.83	−48.72	−4.96	1413.9	0.22
WD J0205−136	6.92	−13.17	−26.62	1712.89	0.07
WD J0715−704	−64.73	2.72	−30.54	1822.5	0.18
WD J2127−221	19.49	−20.95	−20.08	1612.17	0.12
WD J2156−546	−50.52	0.09	15.31	1784.59	0.14
WD0000−186	43.08	−28.07	−3.09	1574.2	0.21
WD0005−163	−47.7	−52.42	−17.08	1378.5	0.26

WD0011+000	−53.89	−58.52	−37.74	1333.9	0.29
WD0013−241	43.68	29.48	16.16	2036.37	0.26
WD0016−220	22.65	−7.06	5.56	1745.03	0.11
WD0016−258	15.78	−14.51	−33.23	1682.72	0.1
WD0017+061	44.89	−4.13	17.15	1776.04	0.18
WD0018−339	−50.06	−34.55	−17.84	1522.12	0.2
WD0024−556	66.23	−42.49	−17.93	1459.61	0.31
WD0027−636	17.49	−1.09	−0.96	1773.83	0.1
WD0029−181	−22.2	−47.7	−30.6	1421.14	0.21
WD0032−175	−83.63	−47.34	−25.03	1421.47	0.31
WD0032−177	−55.87	−46.49	1.73	1428.45	0.25
WD0032−317	−46.09	−22.57	−28.41	1610.11	0.15
WD0033+016	35.48	−9.07	−63.69	1729.54	0.15
WD0047−524	−29.29	−16.26	−13.05	1667.92	0.08
WD0048+202	−29.35	−19.44	−10.36	1650.7	0.1
WD0048−544	−53.33	−17.08	−10.29	1662.4	0.15
WD0050−332	3.0	11.55	1.51	1890.68	0.1
WD0052−147	−6.37	−6.9	−16.5	1745.99	0.01
WD0058−044	−39.9	−7.72	−2.57	1742.25	0.1
WD0102−142	−35.05	7.13	14.54	1861.41	0.11
WD0102−185	46.83	−53.74	−28.27	1376.69	0.3
WD0103−278	−57.32	−65.0	−19.22	1280.58	0.33
WD0106−358	27.37	−10.55	−8.63	1712.48	0.13
WD0107−192	44.14	−11.37	14.92	1712.71	0.18
WD0108+143	−73.99	−24.68	−49.33	1606.44	0.23
WD0110−139	4.35	−6.93	−11.56	1750.81	0.05
WD0112−195	−37.0	−17.09	10.59	1672.48	0.11
WD0114−034	−22.71	−23.92	24.17	1622.51	0.1
WD0114−605	−44.04	−44.78	−33.48	1441.32	0.22
WD0124−257	1.09	−86.53	−5.83	1110.83	0.4
WD0126+101	38.01	−25.84	−33.58	1597.04	0.19
WD0127−050	89.39	−24.17	−19.79	1611.83	0.34
WD0129−205	−62.74	−36.44	−23.53	1512.91	0.23
WD0133−116	−68.84	−48.61	−65.58	1414.3	0.27
WD0137−291	−29.18	−24.14	−0.43	1612.06	0.11
WD0138−236	0.17	−66.79	−5.63	1279.12	0.3
WD0140−392	−41.94	−14.89	−26.02	1681.27	0.12
WD0143+216	21.4	3.66	−16.21	1834.18	0.12
WD0145−221	−15.74	−15.23	−30.72	1680.33	0.05
WD0145−257	−26.53	−48.55	−3.42	1416.66	0.22
WD0151+017	−75.94	−37.92	−20.06	1502.74	0.27
WD0155+069	30.62	31.5	11.57	2067.13	0.23
WD0158−227	−31.26	25.92	20.55	2049.59	0.19
WD0203−138	31.23	−13.69	33.64	1708.58	0.15

WD0204−233	−40.95	−80.68	−60.74	1159.75	0.36
WD0204−306	−21.94	−46.67	−39.46	1428.52	0.2
WD0205−304	−52.48	−63.86	−36.62	1295.1	0.31
WD0205−365	−6.99	−11.99	−19.06	1714.49	0.03
WD0208−263	−77.89	−14.14	−33.99	1702.03	0.23
WD0209+085	−47.43	−13.67	−33.64	1700.54	0.13
WD0212−231	−38.05	−13.09	−2.28	1707.0	0.1
WD0220+222	−66.39	−36.14	−18.62	1521.73	0.24
WD0226−329	43.87	−21.52	0.46	1632.43	0.2
WD0227+050	−2.4	−9.39	5.21	1727.92	0.03
WD0229−481	−17.72	−45.41	14.85	1439.03	0.2
WD0230−144	36.02	−41.57	−2.3	1469.62	0.23
WD0231−054	−39.71	−9.09	−10.26	1731.22	0.1
WD0239+109	1.58	−52.53	−14.98	1386.51	0.24
WD0242−174	−16.32	−9.65	−7.25	1732.82	0.03
WD0243+155	8.61	−3.62	−10.13	1790.49	0.06
WD0243−026	15.7	−52.62	−5.76	1383.65	0.25
WD0250−007	−37.5	−16.13	−27.0	1676.68	0.11
WD0250−026	−19.52	8.11	−29.67	1873.65	0.08
WD0252−350	116.31	−182.09	−51.98	339.92	0.84
WD0255−705	−19.14	−103.55	−3.96	970.74	0.47
WD0257+080	−62.79	−46.79	−0.71	1427.82	0.27
WD0302+027	52.56	−50.18	−64.84	1415.77	0.28
WD0307+149	36.51	−15.25	−21.18	1693.79	0.16
WD0308+188	−13.45	−17.94	−23.13	1667.23	0.06
WD0310−688	10.41	−28.0	−21.6	1573.29	0.13
WD0315−332	−79.24	−12.36	8.37	1746.96	0.22
WD0317+196	−35.49	−3.09	−23.61	1792.43	0.09
WD0318−021	−32.41	2.8	1.14	1834.83	0.09
WD0320−539	26.16	−40.01	−17.36	1478.57	0.21
WD0326−273	−99.47	−52.92	−9.37	1377.86	0.37
WD0328+008	3.41	0.39	7.08	1845.43	0.06
WD0330−009	36.94	5.07	−10.76	1871.28	0.17
WD0336+040	−56.63	−50.67	−26.48	1406.14	0.27
WD0339−035	−71.79	−37.07	−0.62	1513.97	0.26
WD0343−007	1.63	−18.98	11.97	1678.53	0.08
WD0346−011	22.49	−23.67	10.54	1615.63	0.14
WD0352+018	−63.51	−46.57	−12.08	1443.7	0.27
WD0352+049	−24.41	−4.79	−29.96	1784.65	0.05
WD0352+052	78.57	−65.08	44.45	1290.44	0.39
WD0352+096	−47.03	−19.29	−4.55	1651.17	0.14
WD0357+081	53.99	−4.55	−21.44	1766.44	0.22
WD0406+169	−50.86	−18.12	−4.88	1665.32	0.15
WD0407+179	−38.57	−15.07	−17.26	1686.92	0.11

WD0408−041	27.02	−31.39	−13.83	1561.48	0.18
WD0410+117	−24.67	−22.6	−15.83	1627.24	0.1
WD0416−550	−43.97	−34.41	8.64	1532.26	0.17
WD0421+162	−46.28	−19.42	−2.83	1655.19	0.14
WD0425+168	−44.98	−18.98	−2.21	1657.04	0.14
WD0426+106	−57.59	10.59	−5.8	1900.57	0.18
WD0431+126	−46.16	−19.11	−2.95	1658.21	0.14
WD0437+152	−3.56	−18.57	−20.26	1677.42	0.07
WD0440−038	−97.82	−54.31	−61.15	1395.51	0.35
WD0446−789	8.08	−4.84	−19.75	1759.41	0.06
WD0455−282	−37.28	−45.17	−6.39	1451.86	0.21
WD0509−007	−23.76	36.22	−23.02	2115.8	0.22
WD0510−418	−3.98	−18.74	4.52	1674.36	0.08
WD0511+079	1.89	−14.49	−37.73	1691.7	0.06
WD0518−105	−9.88	−31.0	−15.8	1565.99	0.13
WD0548+000	−38.92	−74.5	1.57	1223.81	0.35
WD0549+158	0.85	−47.2	−5.92	1432.8	0.21
WD0556+172	−45.42	−15.89	−5.93	1689.41	0.13
WD0558+165	−37.7	−8.28	−20.21	1748.87	0.09
WD0603−483	−64.79	−25.4	11.37	1615.72	0.19
WD0612+177	−11.38	−59.59	−43.62	1330.83	0.26
WD0621−376	−4.16	−29.57	13.01	1568.78	0.12
WD0628−020	−77.51	−61.48	−27.87	1313.59	0.35
WD0630−050	28.17	0.27	2.04	1824.15	0.14
WD0642−285	−0.77	−27.42	−51.07	1588.14	0.1
WD0646−253	−34.33	−31.49	−11.74	1553.22	0.15
WD0710+216	−26.95	−24.27	−28.8	1615.04	0.11
WD0715−703	−66.54	11.46	−26.67	1891.31	0.21
WD0721−276	19.97	1.68	11.16	1823.38	0.12
WD0732−427	−106.31	−47.19	46.28	1425.78	0.36
WD0752−676	84.98	−42.44	9.36	1458.65	0.36
WD0810−728	−25.14	−26.9	−14.29	1582.43	0.12
WD0830−535	47.28	−16.86	−22.87	1664.24	0.21
WD0838+035	−6.16	1.47	−2.99	1827.27	0.04
WD0839+231	16.24	−23.32	−25.19	1626.2	0.13
WD0839−327	−78.39	−23.62	3.38	1612.97	0.24
WD0852+192	−11.92	−7.87	−21.98	1754.41	0.01
WD0858+160	−68.48	9.84	7.93	1894.2	0.21
WD0859−039	8.21	13.27	−7.76	1911.21	0.11
WD0908+171	−13.54	−4.06	−17.03	1783.18	0.01
WD0911−076	−38.41	−26.48	−13.48	1600.65	0.14
WD0916+064	−47.18	20.22	0.11	2004.51	0.18
WD0922+183	7.9	1.37	−3.81	1827.68	0.07
WD0928−713	−33.83	−72.02	−11.08	1223.64	0.34

WD0937−103	1.66	−15.94	−13.6	1677.22	0.07
WD0939−153	−15.41	−14.03	7.96	1693.29	0.04
WD0945+245	−19.94	−26.8	9.3	1590.53	0.11
WD0950+077	31.72	−24.89	−6.71	1607.67	0.17
WD0951−155	−66.03	18.68	6.9	1963.31	0.22
WD0954+134	22.39	−28.49	−11.32	1585.11	0.16
WD0955+247	−41.31	−56.19	7.16	1356.93	0.27
WD0956+020	4.89	−20.17	38.45	1646.28	0.08
WD0956+045	27.03	−87.05	6.09	1109.05	0.41
WD1000−001	−36.63	−43.84	12.05	1461.38	0.21
WD1003−023	−45.39	2.41	−12.94	1826.89	0.12
WD1010+043	43.81	−52.32	28.67	1387.98	0.29
WD1013−010	−114.14	−53.61	−18.95	1377.99	0.4
WD1015+076	−12.64	−23.76	−28.44	1625.76	0.09
WD1015+161	−43.94	−49.93	−1.67	1408.51	0.25
WD1015−216	−3.78	7.14	−26.54	1863.6	0.07
WD1017+125	−2.07	−6.03	−19.55	1761.23	0.03
WD1017−138	−27.35	−22.56	4.48	1623.51	0.1
WD1019+129	−34.11	−44.32	12.13	1453.02	0.21
WD1020−207	−23.84	−52.5	4.16	1383.59	0.24
WD1022+050	−35.69	−25.95	16.25	1596.39	0.13
WD1023+009	−16.8	−11.75	4.58	1725.09	0.03
WD1026+023	−5.76	−8.58	−18.62	1735.95	0.02
WD1031+063	17.97	−24.14	24.79	1613.25	0.13
WD1031−114	−48.09	−25.47	−24.81	1598.29	0.16
WD1036+085	27.71	−42.58	−4.81	1469.74	0.23
WD1049−158	−29.75	−22.98	5.9	1617.32	0.11
WD1053−092	6.05	−15.5	−10.9	1678.98	0.08
WD1053−290	33.61	−0.09	1.66	1798.79	0.15
WD1053−550	−69.37	−15.14	12.26	1681.69	0.2
WD1056−384	−40.19	−25.23	−4.72	1599.41	0.14
WD1058−129	1.49	6.66	−7.55	1851.35	0.07
WD1102−183	25.8	−35.05	31.55	1517.99	0.18
WD1105−048	17.4	−56.0	−9.05	1354.68	0.27
WD1116+026	−21.36	−14.84	16.05	1682.87	0.06
WD1122−324	−56.96	2.86	−17.77	1823.83	0.16
WD1123+189	−6.0	−22.92	−12.24	1623.01	0.09
WD1124−293	51.27	−16.69	−16.67	1664.92	0.21
WD1125+175	−2.34	−13.27	−14.0	1710.57	0.05
WD1125−025	−27.88	−21.29	2.12	1630.83	0.1
WD1126−222	−50.79	−57.54	−13.83	1340.85	0.29
WD1129+071	−8.65	24.08	−1.52	1995.7	0.15
WD1129+155	12.83	−6.76	6.66	1749.56	0.08
WD1130−125	−16.0	−21.5	−5.08	1627.53	0.08

WD1141+077	−16.96	−47.22	−2.39	1426.33	0.21
WD1144−246	−51.67	−16.26	−28.25	1667.46	0.13
WD1145+187	−8.05	17.19	22.81	1942.51	0.12
WD1147+255	−63.02	−61.96	28.55	1307.02	0.32
WD1149+057	26.3	−24.77	−28.32	1601.12	0.15
WD1150−153	−1.6	−15.97	−16.1	1669.59	0.06
WD1152−287	−17.44	−78.75	29.8	1165.92	0.35
WD1155−243	−23.17	−45.27	−14.09	1438.15	0.2
WD1159−098	−9.96	−50.07	19.08	1399.35	0.22
WD1201−001	−21.26	−23.55	−1.29	1611.76	0.1
WD1201−049	−4.6	−16.39	−9.79	1650.61	0.07
WD1202−232	−0.39	−0.43	14.69	1796.91	0.04
WD1204−136	−51.98	−48.1	−5.58	1415.0	0.25
WD1204−322	−25.13	−4.91	−23.36	1755.7	0.04
WD1207−157	−39.22	−8.77	−16.3	1726.62	0.09
WD1210+140	−52.12	−46.25	1.43	1433.38	0.24
WD1216+036	18.78	−29.12	0.81	1565.54	0.15
WD1218−198	−46.31	−5.84	−27.56	1741.63	0.11
WD1220−292	20.97	4.11	−19.47	1822.28	0.12
WD1229−012	−62.25	−37.09	−1.46	1504.22	0.23
WD1230−308	21.57	−2.72	−2.94	1765.31	0.12
WD1231−141	−38.76	−15.3	−18.94	1672.77	0.1
WD1233−164	−15.74	−31.08	6.5	1546.55	0.13
WD1236−495	−20.01	−42.18	−1.35	1461.94	0.19
WD1237−028	−33.25	−31.95	35.32	1543.05	0.14
WD1241+235	10.12	2.53	−12.75	1821.22	0.08
WD1241−010	10.3	−56.67	−45.26	1342.73	0.25
WD1244−125	−35.73	−18.47	5.39	1650.25	0.11
WD1249+160	61.65	−24.37	−9.01	1601.47	0.26
WD1249+182	−45.0	−11.14	−21.02	1711.49	0.12
WD1254+223	25.26	−61.2	−14.09	1309.9	0.3
WD1257+032	−37.37	−13.81	7.47	1685.12	0.1
WD1257+037	20.48	−90.06	29.47	1078.37	0.41
WD1257+047	−0.41	−48.35	−0.9	1410.97	0.22
WD1300−098	−27.04	−25.57	−3.9	1588.78	0.11
WD1305−017	−50.55	−1.09	5.18	1768.99	0.13
WD1308−301	−4.01	−58.96	6.7	1324.92	0.27
WD1310−305	16.88	−13.47	−10.77	1684.37	0.1
WD1314−067	12.22	−31.82	−15.15	1536.63	0.15
WD1314−153	59.62	−190.97	−50.26	271.99	0.86
WD1323−514	−121.9	−63.84	6.2	1290.35	0.44
WD1326−236	−26.22	−6.02	−13.75	1745.69	0.05
WD1327−083	−42.83	−83.34	6.83	1134.45	0.39
WD1328−152	−20.83	8.29	−7.52	1828.11	0.07

WD1330+036	−28.77	−56.24	−4.73	1345.23	0.26
WD1332−229	16.73	9.81	−19.03	1858.93	0.12
WD1334−160	−20.28	−26.01	0.99	1587.62	0.11
WD1334−678	−52.44	−108.35	−2.16	932.1	0.51
WD1342−237	−12.3	−48.18	22.66	1407.83	0.21
WD1344+106	−73.26	−61.61	−22.64	1306.61	0.34
WD1348−273	44.22	−37.13	−5.95	1498.66	0.24
WD1350−090	57.65	−15.49	0.98	1674.1	0.23
WD1356−233	−58.76	−21.3	−14.14	1627.79	0.18
WD1401−147	−26.64	−51.69	−17.51	1380.73	0.24
WD1403−077	59.77	5.68	−33.04	1812.73	0.25
WD1410+168	88.32	−72.11	−49.16	1217.2	0.44
WD1411+135	17.07	8.71	3.97	1861.67	0.12
WD1412−109	−4.92	−16.51	−6.82	1654.4	0.06
WD1418−088	−83.82	−46.94	−12.72	1422.6	0.31
WD1420−244	−11.2	−2.33	−16.98	1764.58	0.01
WD1422+095	−19.7	−39.67	−15.0	1481.82	0.18
WD1425−811	−22.71	−19.19	−31.5	1645.41	0.08
WD1426−276	62.0	−85.18	−54.35	1104.04	0.43
WD1431+153	−12.06	−13.4	−8.3	1685.68	0.04
WD1434−223	−84.09	16.33	−29.56	1880.59	0.26
WD1448+077	−155.84	−315.57	−30.94	−716.78	0.71
WD1449+168	−1.14	24.72	32.97	1988.13	0.17
WD1451+006	−60.4	−69.09	16.44	1237.39	0.35
WD1457−086	5.04	−11.86	−17.48	1689.35	0.06
WD1500−170	−25.2	−14.76	−34.99	1663.03	0.06
WD1501+032	−54.7	5.82	−10.98	1837.68	0.16
WD1503−093	−24.64	−18.65	−14.98	1645.08	0.08
WD1507+021	5.23	−61.48	13.96	1293.95	0.28
WD1507+220	−39.02	−43.73	−50.58	1444.12	0.2
WD1507−105	−42.74	−20.33	10.03	1628.8	0.13
WD1511+009	6.43	−12.97	−16.23	1674.47	0.07
WD1515−164	33.84	10.42	−14.04	1868.08	0.17
WD1524−749	−96.35	−342.31	−20.05	−916.9	0.55
WD1527+090	4.68	13.05	−6.31	1896.4	0.1
WD1531+184	46.23	−60.9	5.27	1306.3	0.32
WD1531−022	−0.9	−27.61	−10.36	1573.77	0.12
WD1532+033	10.62	1.82	−24.54	1774.06	0.08
WD1537−152	−42.8	−9.85	18.92	1705.62	0.11
WD1539−035	34.79	8.62	−1.11	1861.34	0.17
WD1543−366	−42.42	−1.22	−9.54	1774.26	0.11
WD1544−377	−9.0	−32.27	8.91	1539.92	0.13
WD1547+015	−36.65	−132.34	−82.17	720.72	0.56
WD1547+057	−12.91	−15.34	9.39	1664.56	0.05

WD1548+149	8.21	−18.93	−7.17	1640.71	0.09
WD1550+183	−44.37	−15.14	−2.02	1674.62	0.13
WD1555−089	42.68	−31.95	12.91	1538.42	0.22
WD1609+044	12.08	−12.43	14.54	1684.41	0.08
WD1609+135	89.56	−12.65	31.91	1699.94	0.33
WD1614+136	14.84	−25.0	−12.97	1583.55	0.13
WD1614+160	−46.76	−15.72	−14.85	1662.01	0.14
WD1614−128	70.09	−80.08	8.88	1153.92	0.44
WD1615−154	−24.69	−52.4	−4.25	1373.16	0.24
WD1619+123	14.66	−2.49	−19.51	1773.27	0.08
WD1620−391	17.1	−2.22	−1.24	1778.88	0.09
WD1625+093	72.43	−27.73	21.02	1574.89	0.29
WD1636+057	67.38	−68.67	36.69	1248.31	0.38
WD1640+113	−2.47	−30.42	7.53	1540.73	0.13
WD1655+215	64.83	−13.79	1.55	1687.85	0.25
WD1716+020	−11.89	−96.34	28.78	1026.47	0.43
WD1733−544	3.34	−47.25	−19.42	1420.61	0.21
WD1736+052	65.75	−29.81	−8.25	1558.0	0.27
WD1755+194	62.13	−23.31	−8.45	1602.88	0.25
WD1802+213	50.73	−4.45	29.6	1756.91	0.2
WD1821−131	−83.25	−90.2	−10.59	1076.33	0.46
WD1824+040	80.52	−39.24	25.71	1482.44	0.33
WD1826−045	2.58	−33.84	−18.79	1527.45	0.15
WD1827−106	−34.66	−58.56	−87.81	1321.64	0.22
WD1834−781	−54.51	−106.83	−91.57	943.43	0.45
WD1840+042	−11.74	−8.1	16.37	1730.05	0.01
WD1844−223	−21.7	−4.55	−17.54	1751.76	0.04
WD1845+019	−39.36	−44.69	−8.37	1436.51	0.22
WD1857+119	−65.07	10.32	−17.09	1872.63	0.21
WD1911+135	13.88	−21.2	−15.82	1625.58	0.11
WD1914+094	16.03	−46.97	−10.23	1411.93	0.22
WD1914−598	34.36	−28.48	−18.46	1564.51	0.19
WD1918+110	67.9	6.02	−44.43	1835.6	0.27
WD1919+145	18.25	9.34	−0.57	1875.02	0.12
WD1932−136	9.93	−66.59	−4.38	1253.69	0.31
WD1943+163	54.09	−28.11	−27.37	1573.86	0.24
WD1948−389	−35.08	−28.35	8.36	1556.1	0.14
WD1950−432	−91.92	−33.47	−45.67	1510.7	0.3
WD1952−206	22.73	−84.85	−64.18	1115.98	0.37
WD1952−584	−29.72	−39.69	12.58	1451.92	0.18
WD1953−011	44.05	−22.56	−1.98	1618.49	0.2
WD1953−715	−34.84	−50.35	2.36	1390.0	0.24
WD1959+059	23.17	−49.81	15.96	1395.76	0.24
WD2004−605	−47.7	3.03	2.23	1818.98	0.13

WD2007−219	−27.79	−46.53	−8.1	1426.28	0.21
WD2007−303	58.8	−13.88	−8.11	1689.04	0.23
WD2014−575	18.85	−12.9	−38.83	1689.03	0.1
WD2018−233	−23.95	−13.48	−5.56	1683.08	0.06
WD2021−128	40.38	−24.27	−8.48	1597.28	0.19
WD2029+183	−132.58	−125.48	−27.36	785.43	0.66
WD2032+188	66.21	−6.54	−48.8	1741.09	0.25
WD2039−202	−38.3	−14.77	−18.64	1679.11	0.11
WD2039−682	−14.93	−20.12	−11.93	1637.27	0.08
WD2046−220	−48.17	−13.35	−4.08	1678.67	0.14
WD2051+095	−32.38	29.69	31.92	2025.4	0.21
WD2051−208	−64.41	−26.31	39.11	1586.77	0.2
WD2056+033	4.66	−34.66	17.35	1499.2	0.15
WD2058+181	−41.98	−63.41	−15.04	1287.54	0.31
WD2105−820	−13.57	−38.5	−14.84	1491.26	0.17
WD2115+010	−15.33	11.19	8.38	1874.68	0.09
WD2115−560	−45.53	−21.06	−26.45	1628.62	0.14
WD2120+054	47.64	−80.17	−26.15	1153.83	0.4
WD2122−467	−29.04	−9.11	−15.65	1715.99	0.07
WD2124−224	16.84	−22.3	−17.22	1601.02	0.12
WD2134+218	17.55	4.29	14.67	1833.27	0.1
WD2136+229	−68.22	−49.05	3.31	1404.62	0.29
WD2137−379	−40.3	1.47	13.89	1789.73	0.11
WD2139+115	−66.92	−14.18	−63.29	1679.42	0.2
WD2146−433	39.69	−30.57	14.47	1512.32	0.21
WD2149+021	16.35	−20.53	−18.91	1635.67	0.11
WD2150+021	62.29	2.68	−14.78	1812.07	0.24
WD2151−307	−4.25	−4.89	−7.76	1753.07	0.02
WD2152−045	−15.44	−12.47	−22.56	1687.24	0.04
WD2152−548	−58.17	2.9	24.35	1808.01	0.17
WD2153−419	−39.6	−35.17	−8.57	1495.29	0.18
WD2154−061	28.05	−24.69	−40.31	1593.0	0.15
WD2157+161	−55.44	−40.09	−24.43	1471.01	0.23
WD2159−414	−68.01	−68.66	65.41	1224.18	0.32
WD2159−754	99.22	−46.61	−40.15	1426.68	0.4
WD2200−136	55.8	5.83	−42.29	1834.07	0.23
WD2205−139	−6.66	−2.59	−11.0	1770.79	0.02
WD2207+142	−40.41	25.96	−8.06	2003.85	0.19
WD2211−495	4.0	−20.04	−5.06	1633.29	0.09
WD2220+133	−19.07	−19.44	−1.7	1642.35	0.08
WD2226+061	62.55	3.78	−2.35	1831.11	0.25
WD2226−449	24.22	−29.08	−24.62	1563.88	0.16
WD2235+082	78.76	−5.36	5.08	1761.18	0.29
WD2240+125a	33.63	−6.34	−21.98	1749.94	0.14

WD2240+125b	33.07	−9.16	−19.29	1727.4	0.14
WD2240−017	60.46	−18.05	−18.1	1656.65	0.24
WD2240−045	−181.05	−85.22	−1.16	1092.88	0.63
WD2241−325	−48.64	−20.53	2.86	1623.87	0.15
WD2248−504	−38.87	−38.45	−8.19	1488.27	0.19
WD2253+054	−25.95	−63.68	−0.99	1293.22	0.29
WD2254+126	−49.31	−12.99	−24.07	1696.52	0.14
WD2303+017	−37.67	−7.12	−40.74	1731.79	0.11
WD2303+242	−6.3	−17.02	−12.97	1664.94	0.06
WD2306+124	−4.25	9.7	−3.39	1876.12	0.08
WD2306+130	−24.1	6.12	−11.25	1850.42	0.08
WD2308+050	−39.49	10.27	−8.04	1872.96	0.14
WD2309+105	−41.57	−50.38	6.28	1395.65	0.25
WD2311−260	−3.32	−29.41	−33.64	1545.86	0.11
WD2312−356	−13.66	−0.8	−3.25	1788.25	0.03
WD2314+064	−23.33	−7.37	−10.89	1741.74	0.05
WD2318+126	−81.52	−44.68	4.88	1439.02	0.31
WD2318−226	23.22	−24.33	−17.9	1597.04	0.14
WD2321−549	−17.27	6.33	6.18	1835.35	0.06
WD2322+206	11.81	−10.4	9.51	1719.22	0.07
WD2322−181	−93.88	−39.96	−33.87	1476.3	0.32
WD2324+060	10.01	−52.66	−3.67	1379.86	0.24
WD2326+049	40.12	9.83	−17.79	1881.62	0.19
WD2328+107	39.04	16.5	−17.67	1935.29	0.2
WD2329−332	0.3	−2.47	−10.17	1770.64	0.04
WD2331−475	6.13	−9.52	9.68	1713.36	0.06
WD2333−049	65.24	7.69	−27.55	1864.61	0.26
WD2333−165	6.52	−4.09	−49.36	1768.7	0.06
WD2336+063	−21.58	−3.02	−10.9	1777.16	0.05
WD2347+128	−89.02	−41.73	−2.6	1463.73	0.32
WD2347−192	39.49	10.72	5.13	1883.19	0.19
WD2348−244	53.7	−31.32	−43.09	1550.32	0.24
WD2349−283	−0.39	−25.05	−18.51	1595.88	0.1
WD2350−083	−72.62	−2.19	−43.83	1779.95	0.22
WD2350−248	8.55	1.45	−6.2	1810.47	0.07
WD2351−368	64.93	−178.61	57.52	373.1	0.8
WD2353+026	72.91	−37.34	−8.73	1516.63	0.3
WD2354−151	23.58	−24.88	−15.67	1601.29	0.14
WD2359−324	−171.47	−176.28	−101.12	387.91	0.83
WD2359−434	−2.78	−38.9	−22.84	1489.94	0.17

References

2013, Equatorial coordinate system, `https://quantumredpill.wordpress.com/2013/01/16/equatorial-coordinate-system/`, last access: 04.10.2018

Allen, C. & Santillan, A. 1991, Revista Mexicana de Astronomia y Astrofisica, 22, 255

Althaus, L. G., Córsico, A. H., Isern, J., & García-Berro, E. 2010, Astronomy and Astrophysics Reviews, 18, 471

Bovy, J. 2015, Astrophysical Journal, Supplement, 216, 29

Dalton, G., Trager, S., Abrams, D. C., et al. 2014, in Proceedings of the SPIE, Vol. 9147, Ground-based and Airborne Instrumentation for Astronomy V, 91470L

de Jong, R. S., Barden, S., Bellido-Tirado, O., et al. 2014, in Proceedings of the SPIE, Vol. 9147, Ground-based and Airborne Instrumentation for Astronomy V, 91470M

Dehnen, W. & Binney, J. J. 1998, Monthly Notices of the RAS, 298, 387

DESI Collaboration, Aghamousa, A., Aguilar, J., et al. 2016, ArXiv e-prints [[arXiv]1611.00036]

Edvardsson, B., Andersen, J., Gustafsson, B., et al. 1993, Astronomy and Astrophysics, 275, 101

Evans, R. F. & Dunning-Davies, J. 2004, ArXiv General Relativity and Quantum Cosmology e-prints [gr-qc/0403082]

Fuhrmann, K. 1998, Astronomy and Astrophysics, 338, 161

Fuhrmann, K. 2004, Astronomische Nachrichten, 325, 3

Gaia Collaboration, Babusiaux, C., van Leeuwen, F., et al. 2018a, Astronomy and Astrophysics, 616, A10

Gaia Collaboration, Brown, A. G. A., Vallenari, A., et al. 2018b, Astronomy and Astrophysics, 616, A1

Gaia Collaboration, Prusti, T., de Bruijne, J. H. J., et al. 2016, Astronomy and Astrophysics, 595, A1

Koester, D. 2010, Mem. Societa Astronomica Italiana, 81, 921

Maoz, D. & Hallakoun, N. 2017, Monthly Notices of the RAS, 467, 1414

McCook, G. P. & Sion, E. M. 1999, VizieR Online Data Catalog, 3210

Morales-Rueda, L., Marsh, T. R., Maxted, P. F. L., et al. 2005, Monthly Notices of the RAS, 359, 648

Napiwotzki, R., Christlieb, N., Drechsel, H., et al. 2001, Astronomische Nachrichten, 322, 411

Napiwotzki, R., Christlieb, N., Drechsel, H., et al. 2003a, The Messenger, 112, 25

Napiwotzki, R., Drechsel, H., Heber, U., et al. 2003b, in NATO ASIB Proc. 105: White Dwarfs, ed. D. de Martino, R. Silvotti, J.-E. Solheim, & R. Kalytis, Vol. 105, 39

Napiwotzki, R., Karl, C. A., Nelemans, G., et al. 2005, in Astronomical Society of the Pacific Conference Series, Vol. 334, 14th European Workshop on White Dwarfs, ed. D. Koester & S. Moehler, 375

Nelemans, G., Napiwotzki, R., Karl, C., et al. 2005, Astronomy and Astrophysics, 440, 1087

Pauli, E.-M., Napiwotzki, R., Heber, U., Altmann, M., & Odenkirchen, M. 2006, Astronomy and Astrophysics, 447, 173

Smalley, B. 2005, Memorie della Societa Astronomica Italiana Supplementi, 8, 130

Stroeer, A., Heber, U., Lisker, T., et al. 2007, Astronomy and Astrophysics, 462, 269

Taylor, M. B. 2005, in Astronomical Society of the Pacific Conference Series, Vol. 347, Astronomical Data Analysis Software and Systems XIV, ed. P. Shopbell, M. Britton, & R. Ebert, 29

Turon, C., Primas, F., Binney, J., et al. 2008, Galactic Populations, Chemistry and Dynamics, Tech. rep.

Wyse, R. F. G. 2004, ArXiv Astrophysics e-prints [astro-ph/0402636]

Zhang, X. & Jeffery, C. S. 2012, Monthly Notices of the RAS, 419, 452

Erklärung

Hiermit erkläre ich, dass ich die Arbeit selbstständig angefertigt und keine anderen als die angegebenen Hilfsmittel verwendet habe.

Bamberg, 17.10.2018 _____

Markus Dimpel